mm-Wave Heatsink Antenna Array Design for Low-Sidelobe and Low-Temperature

Ashwath Balasubramanian

TU Delft

mm-Wave Heatsink Antenna Array Design for Low-Sidelobe and Low-Temperature

by

Ashwath Balasubramanian

to obtain the degree of Master of Science in Electrical Engineering
at the Delft University of Technology,
to be defended publicly on 08/10/2021 at 9:30 AM.

Student number:	5142679	
Project duration:	Jan 18, 2021 – Oct 8, 2021	
Thesis committee:	Prof. Dsc. A. Yarovoy,	Professor, Chairman, MS3-EWI
	Dr. ir. M. Mastrangeli,	Assistant Professor, ECTM-EWI
	Dr. Henk Van Zeijl,	Project Coordinator, ECTM-EWI
	Dr. ir. Y. Aslan,	Assistant Professor, MS3-EWI

An electronic version of this thesis is available at `http://repository.tudelft.nl/`.

TU Delft

Abstract

The development of fifth generation (5G) technology is the beginning of a rapid transition in the world of wireless communications. Gbps data rates, minimal latency, and good connectivity are the ultimate aims of 5G. To achieve them, 5G systems employ the mm-Wave frequency band which has a frequency range above 24GHz and so allows for higher bandwidth and gigabit wireless services. Because the size of the antenna elements and their spacings are so small in mm-Wave, massive antenna arrays in the base station may fit into a smaller area while yet providing high gain. However, the problem with mm-Wave integrated antenna array system is the excessive heat generated per unit volume as there is not enough surface area to dissipate heat. Thermal management of antenna system is very important as it affects the reliability and life time of the electronic components in the system. Both active and passive cooling strategies have been employed with passive cooling being the cost-effective and energy-efficient solution. Heatsink antennas can enhance the cooling capacity by providing a dual functionality in terms of both thermal and electromagnetics. Traditionally, most of the works on heatsink antennas are focused at lower frequencies and a few at the mm-Wave frequency range. However, a proper mm-wave thermal modeling in active integrated antennas is missing and there aren't any research on the performance of heatsink antennas in array designs.

This thesis work aims in designing and optimizing a heatsink antenna operating at 28 GHz to achieve a dual functionality. The second aim of the thesis is to develop an appropriate thermal model for the designed antenna. Following the conduction based simulations depending on assumed heat transfer coefficients, proper thermal modeling with appropriate beamformer chip characteristics and a CFD-based natural convective simulation setup has been developed without the assumption of a heat transfer coefficient. Optimal heatsink antenna dimensions are chosen based on the electro-thermal performance. Then, the selected antenna has been used in 1D and 2D arrays. Finally, a comparison study has been made with that of the conventional patch antenna. The results obtained have shown that both 1D (1x8) and 2D (4x4) heatsink antenna array can achieve a better heat dissipation by lowering the junction temperature of about $10-20^{\circ}C$ (for the investigated cases) with higher realized gain and similar side lobe level compared to the respective patch antenna arrays. Furthermore, amplitude tapering of the heatsink antenna array achieved lower side lobe levels which makes this heatsink antenna a low-sidelobe and low-temperature alternative for the patch antenna array.

Acknowledgements

I would want to use this opportunity to offer my heartfelt gratitude to everyone who has supported and assisted me in the completion of my thesis work.

First and foremost, I would want to express my gratitude to Prof. DSc. Alexander Yarovoy, my supervisor, for providing me with this fantastic opportunity to work on my thesis at the Microwave Sensing, Signals, and Systems group. I enjoyed all of your lectures, especially those on Antenna systems and Applied Electromagnetics. I thank you for your support and guidance.

I would sincerely like to thank Dr. Yanki Aslan, my daily supervisor. I cannot express my gratitude enough for the time you spent training me and clearing all my doubts. Thank you for patiently listening to all of my queries and assisting me whenever I had a problem. I appreciate all of your time and effort in supervising me over the last year.

In addition, I'd want to express my gratitude to all of my Microwave Sensing, Signals, and Systems Group colleagues for some intelligent conversations on radars and antennas.

Above all, I'd like to express my heartfelt gratitude to my Mother and friends, who have always been there to listen to me and keep me encouraged during difficult times. Without you all, I would not have been able to accomplish this! I dedicate this thesis to my father. I hope you're having a lovely time in the afterlife. I love you!

Contents

Abstract iii

Acknowledgements v

List of Figures ix

List of Tables xiii

1 Introduction 1
- 1.1 Research Problem Description And Objectives 1
- 1.2 Literature Review 3
- 1.3 Research Approach and Novelty 14
- 1.4 Thesis Outline 15

2 Heatsink Antenna Design - EM Aspects 17
- 2.1 mmWave Patch Antenna Design With Heatsink On Top 17
  - 2.1.1 Comparison With The Regular Patch Antenna 19
  - 2.1.2 Analysis Of X-pol Directivity With Heatsink Dimension 21
  - 2.1.3 Effect Of Removing Heatsink Base 22
- 2.2 Effects Of Geometry And Orientation Of The Heatfins 23
- 2.3 Pattern Directivity With Fin Dimensions 26
- 2.4 Infinite Array Analysis Using Periodic Boundary Condition . . 27
- 2.5 Conclusions - EM Aspects 31

3 Heatsink Antenna Design - Thermal Aspects 35
- 3.1 Thermal Model Considerations 35
  - 3.1.1 Two-resistor Model 35
  - 3.1.2 Properties Of The Electronic Chip Package 36
  - 3.1.3 Thermal Model Of The Antenna 37
- 3.2 Simulation Approaches And Boundary Conditions 38
  - 3.2.1 Conduction Based Model 39
  - 3.2.2 Airflow Model 39
- 3.3 Results And Analysis-Conduction Based Model 41
  - 3.3.1 Analysis With Different h.t.c 42
  - 3.3.2 Effects Of Chip's Parameters On Junction Temperature . . 43
  - 3.3.3 Radiative Heat Transfer 46
- 3.4 Results And Analysis-Airflow Model 47
- 3.5 Conclusions-Thermal Aspects 48

4 Heatsink Antenna - Electro-Thermal Co-Design 51
4.1 Parametric Study With Fin Dimensions 51
4.2 Finite Array Implementation 55
4.2.1 Linear Array Implementation 55
4.2.2 Planar Array Implementation 60
4.3 Conclusion-Electro-Thermal Aspects 62

5 Conclusions And Future Work 65
5.1 Conclusion 65
5.2 Future work 67

A Extended Heatsink Geometry 71

B Calculations For The Thermal Model 72

C Extending Ground plane For Heat Transfer 75

D Additional Parametric Study 76

E Amplitude And Phase Shift Calculations 77

List of Figures

1.1 Fabricated arrays with the Mugen MAX cooling CPU heatsink module (right - single pol., left - dual pol. array). (from [5]) 2
1.2 Fabricated FR4 square patch antenna with heatsink. (from [6]) 3
1.3 Fabricated heatsink antennas with fins parallel to the nonradiating edges (left) and fins parallel to radiating edges (right) (from [7]) 3
1.4 Topology of the heat-sink antenna, cross section view. 1) Heatsink antenna. 2) Heat spreader. 3) Short circuit. 4) Heat exchange surface and radiating surface. 5) Ground plane. 6) Power amplifier circuit-ground plane. 7) Transistor device. 8) Printed circuit board. 9) Surrounding medium. (from [9]) 4
1.5 (Top) Al fractal,n=3 before mounting on substrate. (Bottom left) square patch. (Bottom right) Al fractal, n=3,mounted on FR4. (from [12]) 6
1.6 Cross-sectional view of notch antenna array with radome and printed circuit board. (from [14]) 6
1.7 Massive element antenna array with FSS structure (from [15]) 7
1.8 Thermal deisgn parameters in a unit cell, a)Top view b) bottom view. (from [16]) 8
1.9 Patch Dimension effect on T_{max} with $t_{gnd} = 2mm$ for varying L_{max} (from [16]) 8
1.10 Illustrations of the proposed stamped metal AiP: (a) The cross-sectional view of the entire package. (b) The exploded view of the radiating element. (from [18]) 9
1.11 Temperature distribution of the 8x8 rectangular array a)Case C-1, b) Case C-2, C)case C-3. (from [2]) 10
1.12 Multilayer heatsink structure (Left). Individual antenna element (Right). (from [20]) 11
1.13 Triangular fin heat sink with 120° obtuse angle (Top). Triangluar fin heatsink having alternating layout with 120° obtuse angle. (from [[21]]) 12
1.14 (a) Top view of the vivaldi antenna array with two fins, (b) bottom view . (from [22]) 12

2.1 CST Model of Coaxial fed patch antenna 18
2.2 CST model of patch antenna with heatsink on top 18
2.3 Return loss S11 (dB),(a)Patch antenna,(b)Heatsink antenna 19
2.4 Co-pol pattern directivity (dBi), (a) Patch Antenna, (b) Heatsink Antenna. 20
2.5 Cross-pol pattern directivity (dBi), (a) Patch Antenna, (b) Heatsink Antenna. 20
2.6 Maximum cross pol Directivity (dBi) vs Frequency 21
2.7 Maximum Cross-Pol Directivity (dBi) vs Frequency 22
2.8 CST Model of Coaxial fed patch antenna with heat fins on top 22

2.9 Return loss S11(dB) . . . 23
2.10 Pattern Directivity for the patch with heat fins (dBi) (a) co-pol, (b) cross-pol . . . 23
2.11 Different heatsink antenna geometry and orientations and its Radiation pattern directivity (dBi), (a,b)Rectangular fins parallel to non-radiating edges (PNRE), (c,d) Rectangular fins parallel to radiating edge (PRE), (e,f) Radial pin fins all around the top of the patch, (g,h) Radial pin fins (Edges), (i,j) Radial pin fins (near the center) . . . 25
2.12 Pattern Directivity vs fin height . . . 27
2.13 Pattern Directivity vs Number of fins . . . 27
2.14 Pattern Directivity vs Fin thickness . . . 27
2.15 CST Model of heatfins PNRE array with periodic boundary condition along x axis . . . 28
2.16 Return loss S11 (dB) of infinitely extended heatfins PNRE array,(a)along x,(b)along y . . . 28
2.17 Coaxial feed with a ring inside the air region . . . 29
2.18 Return loss (dB) . . . 29
2.19 Return loss S11 (dB) of infinitely extended heatfins PNRE array with scan angle,(a)15°,(b) 30° . . . 30
2.20 Embedded element pattern of the heat fins (PNRE) antenna with 15° scan angle . . . 30
2.21 Embedded element pattern of the modified heat fins (PNRE) antenna (shrunk patch) with 15° scan angle . . . 31
2.22 CST Model of Radial fins (centre) antenna with Periodic Boundary condition . . . 31
2.23 Embedded element pattern . . . 31

3.1 Two resistor model and its 3D space representation taken from [cite] . . . 36
3.2 4-channel mm-Wave NXP analog beamformer chip from [25] . . . 37
3.3 Thermal model of 4-element Linear patch antenna . . . 37
3.4 Airflow model of 4-element Linear heatsink antenna . . . 40
3.5 Temperature plots for 4-element linear array (a) Patch ,(b)fins (PNRE) heatsink antenna . . . 41
3.6 Temperature plots for 4-element 2D array (a) Patch ,(b)Radial fins (center) heatsink antenna . . . 41
3.7 4-element linear array,(a) T_J vs h.t.c,(b) T_A vs h.t.c . . . 42
3.8 4-element 2D array,(a) T_J vs h.t.c,(b) T_A vs h.t.c . . . 42
3.9 Junction Temperature vs h.t.c at the antenna side (4-element linear array) 43
3.10 Temperature plots for 4-element linear array (a) Patch ,(b)fins (PNRE) heatsink antenna . . . 44
3.11 Temperature plots for 4-element 2D array (a) Patch ,(b) Radial fins (center) heatsink antenna . . . 44
3.12 Temperature plots for 4-element linear array (a) Patch ,(b)fins (PNRE) heatsink antenna . . . 45
3.13 Effects of thermal resistance, (a) θ_{JC} vs T_J,(b)θ_{JB} vs T_J . . . 45
3.14 Temperature plot with radiative heat transfer,(a)Patch,(b)Heatsink . . . 46

3.15 Temperature plot with radiative heat transfer using Anodized Aluminium 47
3.16 Natural convection of 4-element Linear patch antenna 47
3.17 Natural convection of 4-element Linear heatfins (PNRE) antenna 47

4.1 Conduction Based model-Fin height vs (a)Co-pol,(b)Cross-pol 52
4.2 Air flow Model - Fin height vs (a)Co-pol,(b)Cross-pol 52
4.3 Conduction Based model-Fin thickness vs (a)Co-pol,(b)Cross-pol 53
4.4 Airflow model-Fin thickness vs (a)Co-pol,(b)Cross-pol 53
4.5 Conduction Based model-Number of fins vs (a)Co-pol,(b)Cross-pol . . . 54
4.6 Airflow model-Number of fins vs (a)Co-pol,(b)Cross-pol 54
4.7 Array Topology, (a) 1 x 8 Patch, (b) 1 x 8 heatsink antenna 56
4.8 Return loss S11 (dB) of 1 x 8 array,(a)Patch,(b)Heatsink antenna 56
4.9 Realized gain (dB), (a) Patch, (b) heatsink antenna 56
4.10 Farfield realized gain ($\phi = 0$) 57
4.11 Farfield realized gain ($\phi = 0$) for different scan angles 57
4.12 Return loss S11 (dB) of 1 x 8 array,(a)Patch,(b)Heatsink antenna 58
4.13 Return loss S11 (dB) of 1 x 8 heterogenous heatsink antenna array 58
4.14 Realized gain (dB), (a) Patch, (b) heatsink antenna 58
4.15 Farfield realized gain ($\phi = 90$) 59
4.16 Farfield realized gain ($\phi = 90$) for different scan angles 59
4.17 Array topology, (a) 4 x 4 patch, (b) 4 x 4 heatsink 60
4.18 Return loss S11 (dB) of 4 x 4 array,(a)Patch,(b)Heatsink antenna 60
4.19 Realized Gain (dB), (a) Patch, (b) heatsink antenna 60
4.20 Farfield realized gain ($\phi = 0$) 61
4.21 Farfield realized gain ($\phi = 90$) 61
4.22 Conduction based model - Temperature plots, 2D array (a)Patch, (b) Heatsink 62
4.23 2D Heatsink antenna array with scan angle $(\theta_s, \phi_s) = 30°, 45°$ 62

A.1 Extended heatsink geometry (along y) 71
A.2 3D Pattern Directivity (dBi) 71

B.1 Cross-section of the heatsink antenna array 72
B.2 Velocity slice - heatsink antenna array 73

C.1 Extended groundplane (a) Patch, (b) Heatsink antenna 75

List of Tables

1.1 Comparison of different heatsink antenna topologies 13

2.1 Comparison of EM performance 20
2.2 Comparison of EM performance for different heatsink geometries and orientations 24
2.3 EM performance comparison of the selected heatsink orientations . . . 26

3.1 Chip parameters from [5] 37
3.2 Geometry properties 38
3.3 Comparison of the two heat transfer simulation models 48

4.1 Comparison of joint EM-thermal performance 57
4.2 Comparison of joint EM-Thermal performance 59
4.3 Comparison of joint EM-Thermal performance (4 x 4) array 61

B.1 Thermophysical properties of Air 73

D.1 Parametric study data 76

1 Introduction

This chapter deals with the background on the research project and the general outline of the thesis work. Motivation to do research, problem description, and research objectives will be discussed in the first section. Next to this, a literature survey on existing state-of-art techniques for thermal management in antennas will be discussed. In the third section, the chosen research approach and novelty of the thesis will be elucidated. Finally, in the end, the thesis outline will be provided.

1.1. Research Problem Description And Objectives

The rapid transformation in the world of wireless communications starts with the development of fifth generation (5G) technology. The ultimate goals of 5G are to achieve Gbps data rates, low latency, and excellent connectivity. To achieve this, 5G systems use mmWave frequency band with frequency range beyond 24GHz as this provides larger bandwidth and gigabit wireless services. The advantage of mm-Wave is that the size of the antenna elements and their spacings are so small that large antenna arrays in the base station can fit into a smaller area providing high gain [1].

However, the small aperture size of antenna array will not provide sufficient surface area for the heat to dissipate. In mm-Wave, the excessive heat generation per unit volume within the integrated antenna array system is a serious problem as it negatively affects the reliability and stability of the electronic components in the RF circuitry. For example, at mm-Wave the power generated is about $2W$ in just $4cm^2$ area of the chip.[2]

It can be stated through the Arrhenius equation that for every $10°C$ rise in Integrated Circuit (IC) junction temperature, the average lifetime of the chip gets reduced by 50% [3]. This shows that cooling such systems is very much necessary to have a better lifetime of the electronic components. Cooling of such systems involve either active cooling, passive cooling or both (hybrid). Active cooling depends on external devices such as fans, pumped liquids to enhance the heat transfer employing forced convection whereas passive cooling achieves a natural convective heat transfer utilizing heatsinks, heat spreaders, and thermal interface materials. The use of external fans or liquids for

actively cooling the electronics requires more energy and cost. On the other hand, with passive thermal management no external energy is required and it is a cost-effective and energy-efficient solution.

The cooling issues at the Ka frequency band where the current 5G mmWave operates has been dealt by employing active cooling techniques using fans or liquid pumps [4]. For 5G base station antennas, reducing the cost, maintenance requirements, and energy consumption while increasing the reliability is crucial. Therefore, fully passive cooling solutions are desirable. Currently, to achieve this, large-sized metallic heat sinks are attached to the beamformer chips at the back of the antenna. An example of such heatsink is shown in Figure **1.1**. The disadvantage of such large heatsink is that they are bulky and occupy a lot of space.

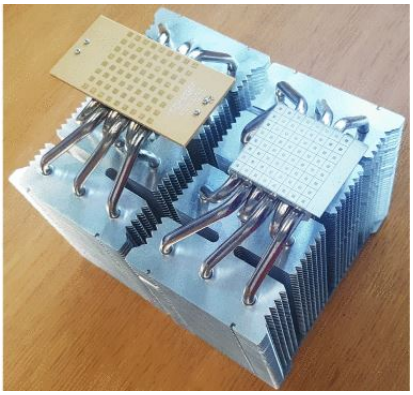

Figure 1.1: Fabricated arrays with the Mugen MAX cooling CPU heatsink module (right - single pol., left - dual pol. array). (from [5])

However, without attaching a large heatsink at the bottom surface of the chip, heat will not dissipate and forced convection techniques have to be used for the cooling of such structures. Therefore, low-profile antenna passive thermal management is a major research problem. To achieve this, heatsink antennas can be used which are 3D radiating structures that create additional heat flow paths from the beamformer chips to the surrounding air. They have the potential of providing dual-functionality in terms of both thermal and electromagnetics. This way, the requirements on the size and weight of the bulky metallic heatsinks attached to the chips can be relaxed.

The main objectives of the thesis are as follows.

1. To design and optimize such heatsink antenna centered at 28 GHz operating frequency for dual functionality and to analyze its performance both in terms of electromagnetics and thermal aspects.

2. To design a proper thermal model with the beamformer chip and evaluate the thermal performance of the designed mmWave antenna.

3. To realize such elements in 1D/2D arrays and investigate their scanning range abilities and mutual coupling effects as well as the thermal performance of the arrays.

4. To compare the electromagnetic and thermal performance of the designed heatsink antenna with the conventional microstrip patch antenna and with the relevant alternatives proposed in the literature.

1.2. Literature Review

A comprehensive list of articles on heatsink antennas has been presented here where some of the literature use a regular antenna like patch and a heatsink attached on it for dissipating the heat, while other use different approaches so that the antenna (or its layout in an array arrangement) itself acts as a heatsink.

Antenna+Heatsink:

L.Covert and J.Lin (2006) in [6] suggest a new type of antenna which considers the dual functionality aspects both electromagnetic and thermal. A simple edge-fed patch antenna centered around 2.4 GHz has been considered for the design and the effect of placing a heatsink on the patch was analysed. The input reflection coefficient results show that there is a decrease in the resonant frequency to 2.26 GHz(Measured), 2.23 GHz(Simulated) due to the increase in effective length of the patch. The radiation efficiency of the antenna has been greatly improved due to the less confinement of the electric fields in the substrate. This resulted in a higher peak realized gain for the patch with heatsink.

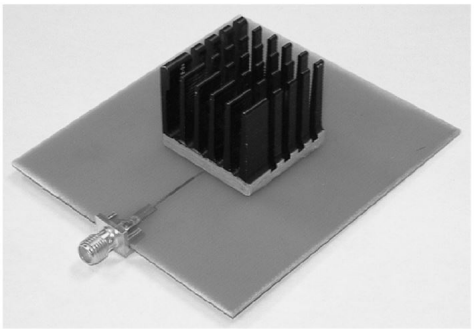

Figure 1.2: Fabricated FR4 square patch antenna with heatsink. (from [6])

L.Covert et al.(2007) in [7] proposed the use of extruded pin heatsinks having two different orthogonal orientations. Two 5.8 GHz heatsink antennas were designed, one with the extruded fins parallel to the non-radiating structure (Fins PNRE) and the other is with extruded fins parallel (Fins PRE) to radiating edges.

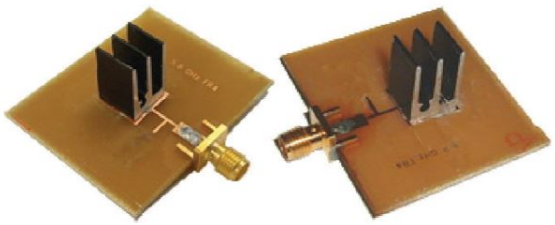

Figure 1.3: Fabricated heatsink antennas with fins parallel to the nonradiating edges (left) and fins parallel to radiating edges (right) (from [7])

A silver conductive epoxy layer is used between the patch and heatsink to improve the thermal conductivity. Tuning stub is used only in the heatsink antenna case for impedance matching, where its length and placement are determined experimentally. Results show that there is increase in radiation efficiencies for both the cases (Fins PRE) and (Fins PNRE) compared to the normal patch. The return loss (S11) dB shows a huge improvement in the 10 dB bandwidth from 3.1% (basic patch) to 17.6% (PNRE) and 11.9% (PRE). However a better comparison is made measuring the Q of the antenna with the same matching network for all cases. The basic patch had higher Q value compared to the heatsink cases. Comparing the peak directivity and gain for the three cases, it was found that (Fins PNRE) case had better directivity than the patch since the fins are parallel to the current flow on the patch whereas in Fins PNRE it was the opposite case (perpendicular to current flow) which resulted in a lower directivity than the patch for the Fins PRE case.

Later, L.Covert et al. in [8] demonstrate the performance of the heatsink antenna by integrating the above heatsink antenna with Power Amplifier with a thermal via between power amplifier and the heatsink. It is stated that a high thermal conductivity material can be used for the via to dissipate heat better. This has an impact on the resonant frequency, which can be easily compensated by adjusting the patch length. As the via is at the center of the patch, there is no negative impact on the shape of the radiation pattern. The performance of RF devices is strongly influenced by the temperature increase due to the heat dissipation. Therefore, an active heatsink antenna for RF transmitter has been proposed by A.Alnukari et al. in [9]. Higher thermal conductivity and bigger surface area helps for better heat dissipation in the transmitter.

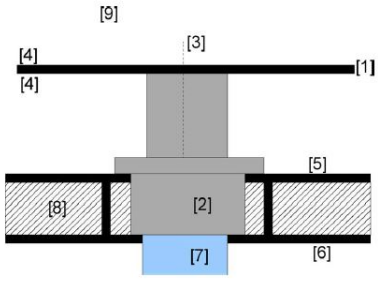

Figure 1.4: Topology of the heat-sink antenna, cross section view. 1) Heatsink antenna. 2) Heat spreader. 3) Short circuit. 4) Heat exchange surface and radiating surface. 5) Ground plane. 6) Power amplifier circuit-ground plane. 7) Transistor device. 8) Printed circuit board. 9) Surrounding medium. (from [9])

Figure **1.4** gives the topology of the proposed heatsink antenna where FR4 epoxy substrate with $1.58mm$ thickness and copper with metal thickness of $35\mu m$ has been used. Wire fed Patch antenna designed for 2 GHz with diameter $1mm$ is used to feed the patch with $67mm$ x $54mm$ dimensions. The conducting cylinder connecting the power amplifier circuit to the patch antenna is the heat spreader which is effective in creating a thermal path for heat dissipation. About 10 mm diameter is used for the heat spreader as increasing the heat spreader diameter larger than the wavelength might

affect the electromagnetic performance. Thermal simulations using Finite element method results matched with the Infrared thermography measurement. Relation between the copper thickness and thermal resistance was shown where as the copper thickness increases, the thermal resistance drops down.

A.Alnukari et al. extended their work in [10] and [11] where [10] present an approach of cooling the antenna using a distilled water channel and [11] use a sapphire layer for cooling. Results show that the distilled water which is about $20°C$ removed about $0.73W$ of thermal power/cm^2 of the antenna whereas it was $0.28W$ for the case without distilled water. Experimental verification was done by infrared imaging which proved the simulation correct. With the sapphire layer having permittivity of 8.9, the heat removed was about 1W /cm^2 of the antenna while the thermal resistance was about $5.5°C/W$. Temperature distribution results show that the antenna maximum temperature reduced from $140°C$ to $80°C$ with the effect of sapphire layer.

In [12], J.Casonova et al.(2008) suggest an increase in surface area of the heatsink to improve the heat dissipation thereby preventing burnout. A 3D fractal structure has been proposed with a cube of side w and for every iteration there is an addition of cubes of side $w/2^n$ with centre on each corner and these fractals are placed on top of the patch. From n=0 to n=4, the fractals were designed and a comparison is made in terms of thermal and electromagnetic properties. The design from [7] (Fins PNRE and Fins PRE) were also considered for comparison. With the operating frequency set to 5.8 GHz, electromagnetic properties were compared and it is seen that all the heatsink antennas had increased radiation efficiency compared to the patch. The resonant fequency shift is observed for each cases and with n=1 it increases up to 6.75 GHz due to the decrease in effective length. Similar radiation patterns were observed in all the cases but the beamwidth in E-plane varies. The orientation of the main beam showed variation for different cases. Also, a change in linear polarization (patch) to the elliptical polarization for fractals was observed.

At steady state, thermal resistance was calculated by simulation under natural or forced convection scenario. This was done to characterize the heatsink performance. It is observed that except for n=0, all the other fractal heatsinks showed less thermal resistance than the extruded pin-fin heatsinks. This is due to the fact that as n increases, the surface area of the heatsink increases resulting in better heat conduction. However there is also some increase in cross-sectional area of the antenna as n increases. So, with a constant volumetric flow rate, the air speed increases resulting in better convection.

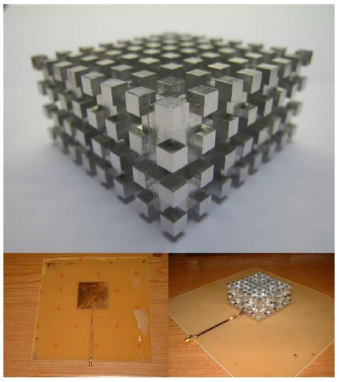

Figure 1.5: (Top) Al fractal,n=3 before mounting on substrate. (Bottom left) square patch. (Bottom right) Al fractal, n=3,mounted on FR4. (from [12])

Antenna as a Heatsink / Layout optimization as a heatsink:

A Solder based self assembly (SBSA) technique has been advocated in [13] as a robust and novel technique for integration of 3D antennas. Both at low (2.4 GHz) frequency and high (23.8 GHz) frequency the two 3D antennas, 3D cube antenna and 3D TSP Antenna were compared with the conventional patch antenna with heatsink on top. The three-dimensional constructs were made up of an array of three-dimensional cubes.On a scale of 300 μm in three dimensions, a 3x3 array was developed on the patch substrate. The patch is 2.87mm X 2.87mm in size. On the substrate, truncated square pyramids with a 150m square base and a 75 m height were built in a 3 X 3 array. In self-assembly experiments, truncated structures yielded the highest yield, so they were used to model the 3D antenna. Results show that the 3D cube antenna and the 3D truncated structured antenna had better gain and radiation efficiency.

A new approach of using stepped notch antenna array as heat fins is presented in [14]. A radome is placed above the notch antenna array for trapping the air such that it reduces the thermal resistance. A 26 x 11 array for Ku band has been designed where the actual radiating elements are 24 x 8. Thermal analysis show that the array is competent of giving up to 0.4°C/W thermal resistance.

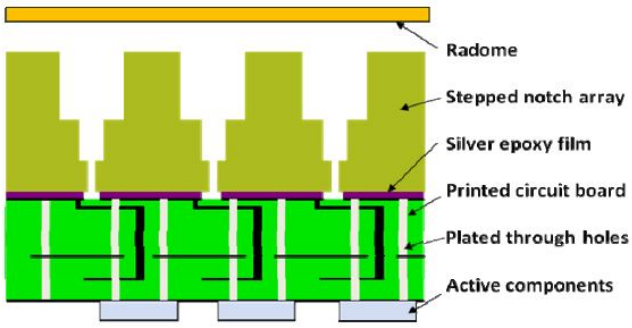

Figure 1.6: Cross-sectional view of notch antenna array with radome and printed circuit board. (from [14])

In recent times, different approaches for better heat transfer enhancement in the antennas at the mm-Wave frequency range have been introduced.

Massive MIMO antennas are required to achieve large capacity communications for 5G. This leads to large amount of heat dissipation for which the antennas would require the placement of heatsink to the beamformer chips at the back of the antenna. NEC [15] suggest an alternative approach for dissipating heat efficiently which reduces the size of heatsink and thus reducing the entire antenna array size. Two new features of this technology were to exploit the antenna itself to dissipate heat along with the heatsink and providing a thermal pathway for better dissipation of heat. For the dissipation of heat from the antenna element, the surface area has been expanded and Frequency Selective Structure (FSS) has been placed to act as additional heat dissipation fins. FSS structure has been selected as it allows only specific frequencies to pass through thereby making them electromagnetically transparent. For better heat transfer, a split ring structure is considered reducing the total size of the array and vertical orientation of the antennas with checker plate style pattern arrangement for enabling good air flow. The structure is shown in Figure **1.7**.

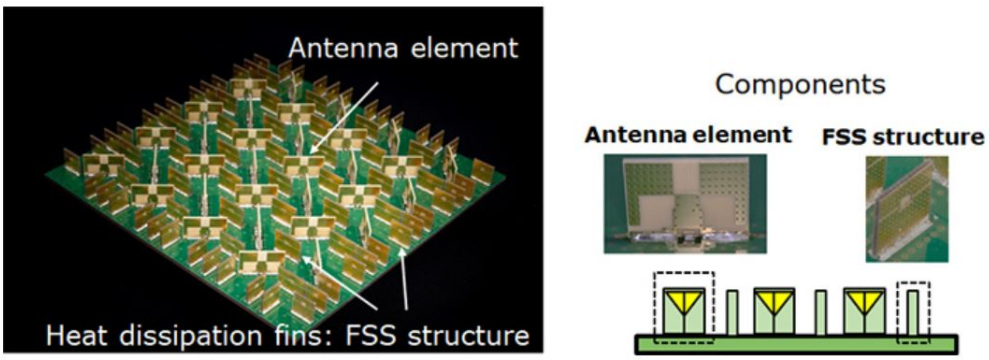

Figure 1.7: Massive element antenna array with FSS structure (from [15])

By varying the thickness of the ground plane and the aperture size of the antenna array, Y. Aslan et al. in [16] studied the thermal and electromagnetic properties of the antenna array at mm-Wave frequency. Figure **1.8** gives the thermal model design. For the EM model, Patch antenna is used which is fed by a 50 ohm microstrip feeeding line on the chip substrate and it is connected with the patch through a vertical feeding pin. For the thermal model, two -resistor model [17] has been used where it consists of three nodes (Junction, Case and Board) connected by two thermal resistors (junction-to-case and junction-to-board). Here the heat flow is either through the Case or Board node and not through the sides.

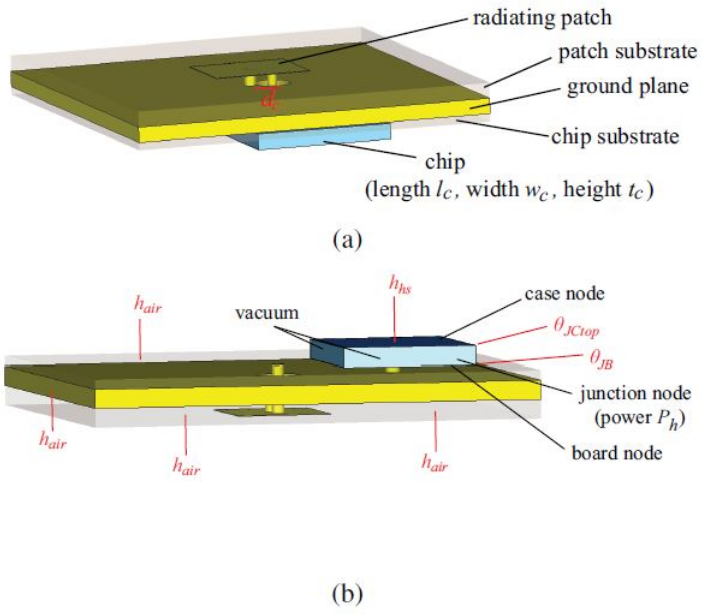

Figure 1.8: Thermal deisgn parameters in a unit cell, a)Top view b) bottom view. (from [16])

An 8x8 array has been designed and the thermal simulation results show that as the ground plane thickness is varied from 0.05mm to 2mm, the maximum junction temperature (T_{max}) decreases. It is observed that the effective thermal conductivities in lateral and vertical directions increased with the increase in ground plane thickness. Effect of varying the aperture size has also been studied. However, for thinner ground plane the variation of the aperture size (L_{max}) doesn't significantly reduce the temperature. EM performance has been computed for the best and worst cooling scenario, where it is found that patch dimensions need to be changed to compensate the effect of mutual coupling. Figure **1.9** gives the table showing the effect of patch dimension on the junction temperature.

$L_{\max}$ (λ_0)	$T_{\max}$ (°C) (L_p = 3.20 mm, W_p = 2.50 mm)	$T_{\max}$ (°C) (L_p = 3.26 mm, W_p = 1.80 mm)
5	153.4	153.7
7.5	142.7	142.9
10	133.5	133.6
12.5	126.2	126.2
15	120.5	120.6
17.5	116.3	116.4
20	113.0	113.0

Figure 1.9: Patch Dimension effect on T_{max} with $t_{gnd} = 2mm$ for varying L_{max} (from [16])

A new approach for better heat dissipation for phased array applications has been studied by Junho park et al. in [18], where metal stamping technology is used for the Antenna in package (AiP) concept. This approach proposes the use of RFIC and antennas to be mounted on the same side. Planar Inverted-F antenna (PIFA) is consid-

ered for their large aperture size, wide feeding structure and easy realization through the stamping process.

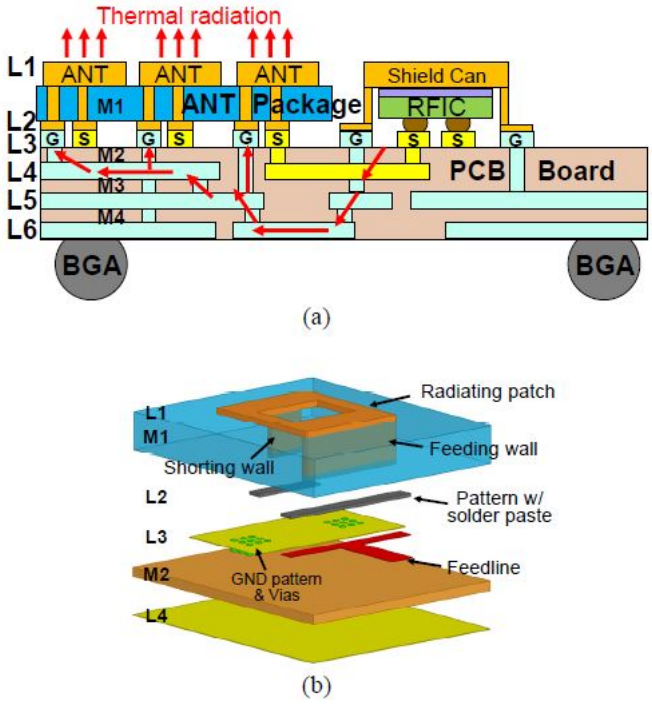

Figure 1.10: Illustrations of the proposed stamped metal AiP: (a) The cross-sectional view of the entire package. (b) The exploded view of the radiating element. (from [18])

1 x 8 patch antenna has been designed through stamped metal AiP at the centre frequency of 28 GHz. Conduction based analysis with $10 W/m^2K$ heat transfer coefficient show that maximum temperature was $11°C$ less than that of the maximum temperature in a conventional patch array topology.

The problem of thermal control in 5G base station antenna arrays at mm-waves has been solved by Y.Aslan et al. in [2]. For the first time, it has been proposed to use passively cooled planar AESAs with fanless CPU coolers as an energy-efficient and relatively low-cost solution with a significant beamforming flexibility. Sparsity has been implemented into antenna layouts by increasing inter-element spacing in order to improve cooling efficiency. A number of sparse array topologies have been proposed and their thermal and electromagnetic efficiency evaluated.

With the 8x8 normal square array, a parametric analysis of the maximum junction temperature was conducted, varying the heat dissipated $P_h(W)$, h.t.c of the passive cooler $h_{hs}(W/m^2K)$, and the spacing between the elements (d_e). Figure **1.11** shows the temperature distribution of the regular 8x8 square array layout for a varying inter-element spacing. Here, Case C-1,C-2,C-3 has spacing $0.5\lambda, 1\lambda, 2\lambda$ respectively with $P_h = 2W$ and $h_{hs} = 1000 W/m^2K$

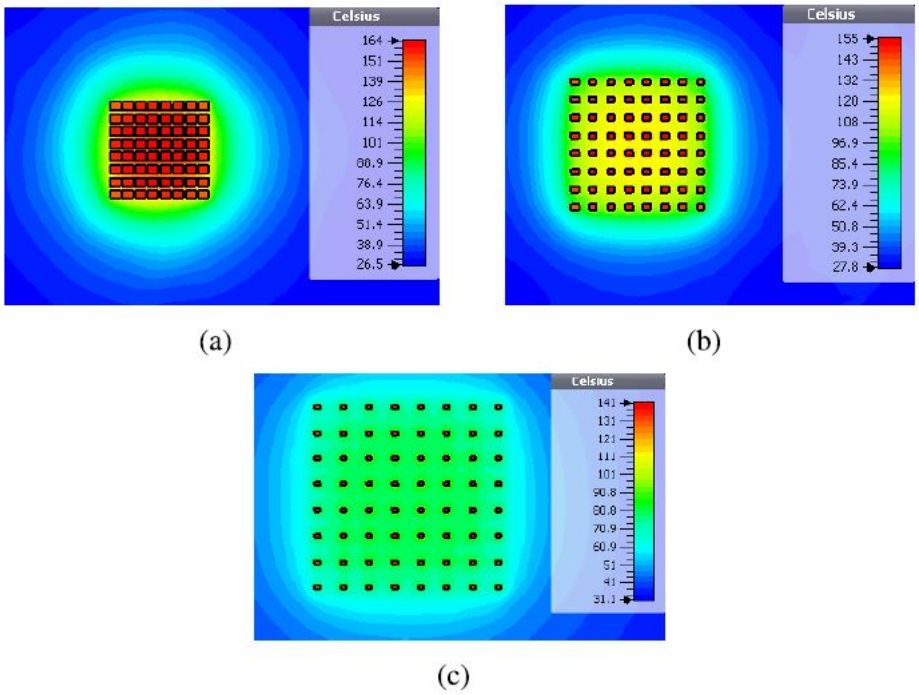

Figure 1.11: Temperature distribution of the 8x8 rectangular array a)Case C-1, b) Case C-2, C)case C-3. (from [2])

However, with the increase in spacing, undesirable grating lobes occur which is a trade-off. So, alternative array layouts like sparse array, spiral array, thinned array, sparse circular ring array and Heatsink antenna array topologies were considered and its thermal performance has been simulated.

Comparisons of the junction temperature with the alternating layout has been made where it is found that these alternating layouts achieved better Electromagnetic performance while maintaining its cooling. The average distance between the elements was found to be the most important factor in lowering the temperature for the various sparse topologies. The sunflower topology was found to be the best in this regard, as it allows for the largest inter-element spacing of all investigated topologies while maintaining low side lobe levels.

[19] suggest a large-scale (256-element) aperiodic array topology for future 5G/6G communications. The addition of more elements resulted in an increase in gain and the reduction of side lobe level. This increase in elements also decreased the heat produced per element for the same EIRP performance. Through conduction-based thermal simulations, it was shown that large sparse arrays can help in reducing the heat generated per unit volume thereby getting rid of the heatsink attached at the back of the array.

[20] present a 60 GHz Heatsink antenna array fabricated by 3D printing where the fin heatsink is soldered on a low-temperature cofired ceramic (LTCC) substrate with a chip mounted at the bottom. An open-ended waveguide and two vertical metallic fins make up the antenna part, which is shaped like a horn. The proposed heatsink antenna

array, according to simulation and calculation, not only performs well in terms of radiation but also has a strong heat dissipation capability. Figure **1.12** gives the multilayer heatsink antenna array structure and the single antenna element

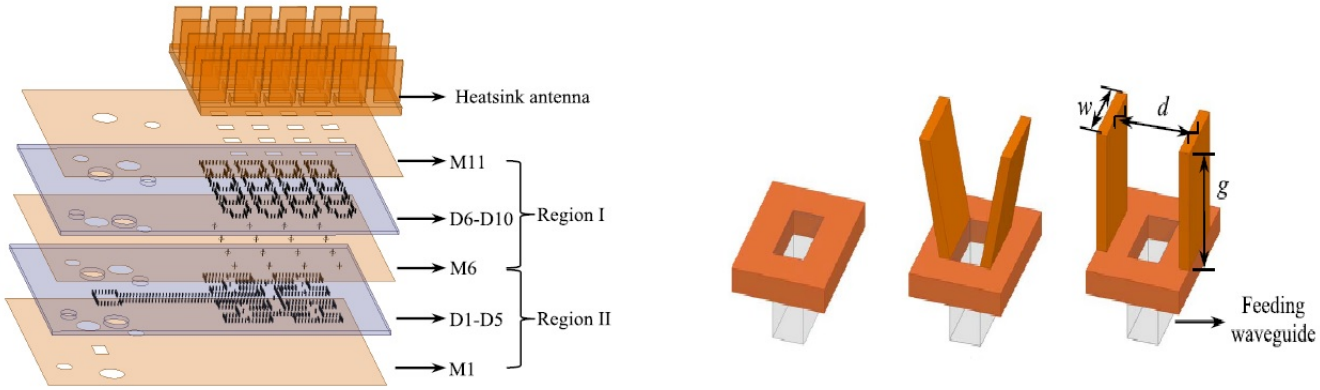

Figure 1.12: Multilayer heatsink structure (Left). Individual antenna element (Right). (from [20])

The (4x4) antenna array's feeding network is made up of two-layer substrate integrated waveguides (SIWs) with various metallic vias, and the 3-D printed heatsink is installed on an LTCC substrate. Metal layers are denoted by M1–M11 in the LTCC substrate, while ceramic layers are denoted by D1–D10 from the bottom up. A step-profiled transverse electromagnetic mode (TEM) horn structure is constructed as the antenna portion by combining the fins with an open ended waveguide, as shown in Figure **1.12**. Parametric studies of pattern gain with fin width, fin height and spacing between the fins has been conducted to determine the best suited dimensions. Furthermore Electrothermal analysis has been made now with the parametric study of the hotspot temperature. The dimensions of the fins are chosen based on better EM and thermal performance. The hotspot temperature dropped as the fin height and width increased, indicating that the surface area expanded, resulting in better heat dissipation.

The chip's dissipated power is $0.2W$. Since the heatsink structure is exposed to the air, the convection boundary in thermal simulation is set to $h = 10W/(m^2K)$ at $300K$ ambient temperature. The entire structure's hotspot temperatures are shown to be 313.1 and $353.2K$, respectively. The fin-shaped heatsink on the LTCC package achieves a temperature reduction of 40.1 K. The thick metallic vias of SIWs in the LTCC substrate act as thermal spreaders by default, providing an efficient means of transferring the chip's dissipated thermal energy to the heatsink.

The structure of the heatsink plays an important role in thermal management where [21] compare different layout of the heatsink with its thermal performance. About 5 different heatsink layouts were compared, Rectangular fins, Triangular fins with right angle , obtuse angle and alternating triangular fins with right angle, obtuse angle. It is

seen that the effective Heat Transfer Coefficient (HTC) has been improved for all the cases relative to the rectangular fin case. The alternating triangular layout with obtuse angle had the maximum increase in HTC about 12.1% relative to the rectangular fin case. CFD analysis show that in the alternating trainagular fin case, increase in the angle θ reduced the temperarture at the base and the fins. Optimal angle was chosen to be 150° since a further increase in the angle θ after 150° resulted in reduced fin efficiency.

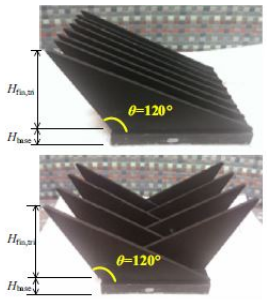

Figure 1.13: Triangular fin heat sink with 120° obtuse angle (Top). Triangluar fin heatsink having alternating layout with 120° obtuse angle. (from [[21]])

In [22], a vivaldi antenna array has been designed to show better heat dissipation and electromagnetic radiation capabilities. Here, the vivaldi antenna is manufactured with the help of 3D printing technology where Substrate integrated Waveguide (SIW) with a longitudinal slot is used as the feed for the antenna. A 1x4 Vivaldi antenna array designed achieved a bandwith of 28.72% (21.63-28.81 GHz) and a gain range of 10.5-12.5 dBi. In addition to this a fin shaped structure is added in the array as shown in Figure **1.14** where the metallic fins are parallel to the E-field of the pattern which according to image theorem can enhance the directivity. Also this fin shaped structure can enhance heat dissipation as it provides more surface area.

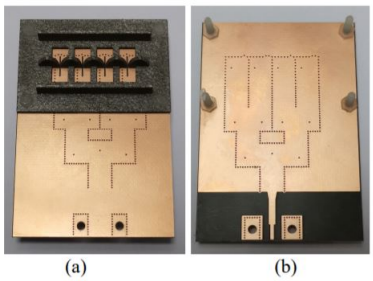

Figure 1.14: (a) Top view of the vivaldi antenna array with two fins, (b) bottom view . (from [22])

The thermal validation is done using COMSOL where a silicon chip with 0.5 W dissipated power is condiered as the heat source and a heat transfer coefficient of $h = 10W/(m^2.K)$ at $300K$ ambient temperarure is considered. About $18K$ reduction is hotspot temperature is observed.

Most research papers use a conduction-based simulation with $10W/(m^2K)$ h.t.c in the solid-air area, whereas a few papers include experimental results and others simply explain the theory.

Type	Ref	Antenna Topology	Frequency (GHz)	Number of Elements	Peak Gain (dB)	-10dB Impedance Bandwidth (GHz)	Heat dissipating structure / technique
Antenna+Heatsink	[6]	Heatsink-loading microstrip patch	2.4	1	4.12	0.04 (1.76%)	Fin-shaped heatsink
	[7]	Heatsink-loading microstrip patch	5.8	1	6.25	1.02 (17.6%)	Fin-shaped heatsink
	[9]	Air-dielectric microstrip patch	2	1	5	0.07 (3.5%)	Patch with heat spreader
	[10]	Air-dielectric microstrip patch	2	1	3.85	0.03 (1.5%)	Patch with heat spreader & distilled water channel.
	[11]	Air-dielectric microstrip patch	2	1	4.06	0.03 (1.5%)	Patch with heat spreader & sapphire layer
	[12]	3-D fractal heatsink -loading microstrip patch	1.43	1	7.15	0.04 (2.80%)	3-D fractal heatsink
Antenna as a heatsink	[13]	3D cube antenna	23.78	1	4.89	1 (4.2%)	SBSA 3-D structures
	[14]	Stepped notch antenna array	13.2	24 x 11	-	5 (37.88%)	Stepped notch array with radome
	[18]	Planar inverted -F antenna	28.5	1 x 8	13.78	0.7 (2.45%)	Stamped metal AiP
	[20]	Open-ended waveguides in heatsink	60	4x4	18.8	7 (11.7%)	Fin-shaped heatsink with numerous thermal vias
	[22]	3-D Vivaldi Antenna	25	1x4	15.5	7.2 (28.8%)	Vivaldi Antenna and Fin-shaped heatsink
Layout optimization as a heatsink	[16]	Microstrip patch array	28	8 x 8	22.68	1.7 (6%)	Thick ground plane and large aperture size
	[2]	Sunflower array	28.5	64	24.6	-	Aperiodic arrays (Larger inter element spacing)

Table 1.1: Comparison of different heatsink antenna topologies

Based on the comparison of different heatsink antennas made in [20], [22] a comparison table of different antenna topologies and the heat dissipating technique is shown in Table **1.1**.

Conclusions:

To summarize, research works on heatsink antennas fell into three categories, antenna as a heatsink, heatsink+antenna and layout optimization as a heatsink. Both active and passive cooling approaches for thermal management in antennas has been used in various studies. Previous research on heatsink antennas has mostly focused on low frequencies, with only a few studies at mm-Wave frequencies examining the effects of heatsinks on standard patch antennas and other approaches to antenna thermal man-

agement. Return loss, pattern gain, directivity, and radiation efficiency are all shown as EM results for these heatsink antennas. A conduction based simulation with the assumption of heat transfer coefficient is used for thermal simulations in most of the research works. However, there are few things that hasn't been explored in the literature.

- The proper mm-wave thermal modeling in active integrated antennas is missing
- The usefulness and performance trade-offs of heatsink+antenna concepts in mm-wave bands are not known.
- The optimality of the proposed heatsink antennas in terms of joint electromagnetic and thermal performance is not clear
- There is lack of studies in performance investigation of heatsink antennas in array configurations
- The effects of heatsink antennas on cross-polarization and scanning abilities of the heatsink antenna array has not been investigated
- At mm-Wave frequencies, the interference problem due to high sidelobes in heatsink antenna array has not yet been addressed.
- In the thermal simulations of the preceding studies involving passive cooling, a conduction-based heat transfer or natural convection heat transfer with an h.t.c value assumption was used. Nonetheless, thermal simulations must have the accurate determination of h.t.c value for natural convection and also involve heat transfer through radiation which would give close to accurate results with the natural scenario

1.3. Research Approach and Novelty

The antenna+heatsink strategy is chosen from among the three approaches for thermal management in antennas due to its straightforward applicability to the existing prototypes. All of the research conducted under this approach is focused at low frequencies. However, at high mm-wave frequencies, overheating becomes a severe issue and need to be addressed.

- For the first time, a novel design of mm-Wave heatsink antenna is investigated in this thesis project. With the designed heatsink antenna, the effects of heatsink dimensions, different orientations on both the EM and Thermal performance are explored.
- A novel thermal model considering appropriate beamformer chip parameters is developed. The developed antenna thermal model is then simulated using an unique CFD-based natural convection scenario setup that does not make any assumptions about heat transfer coefficient values.

- The influence of h.t.c. and thermal resistance on junction and antenna temperatures are researched. The patch antenna is used as a benchmark, and a novel comparison is done between patch and heatsink antennas in terms of EM and thermal performance.
- Based on the results of the parametric study, optimum fin dimensions are selected for the array design. Another novel aspect includes the examination of scanning abilities, mutual coupling, sidelobe level, and junction temperature of such antennas in finite and infinite arrays.

1.4. Thesis Outline

The outline of the thesis is the following:

Chapter **2** presents the design of mmWave patch antenna and heatsink antenna designs. The electromagnetic performance between the two designed antennas has been compared. Focus is given at examining the maximum Co-polarization and Cross-Polarization Directivity for different heatsink geometry, which helps in modification of the designed heatsink antenna. Effects of different orientation of heatsink antenna has been discussed and comparison in terms of EM aspects were done. Finally, infinite array analysis of the designed heatsink antenna has been done in order to check the mutual coupling effects and embedded element pattern for very large arrays.

Chapter **3** consists of the detailed thermal modelling of the designed structure considering appropriate parameters of the NXP beamformer chip which is used as the heat source. The assumptions and boundary conditions for the conduction based heat transfer with the assumption of heat transfer coefficient and air flow model are stated. The models are simulated to obtain the maximum junction temperature at the chip. The change in junction junction temperature and temperature at the antenna has been observed for different values of heat transfer coefficient. Results from the air flow natural convective model without the assumption of heat transfer coefficient are also obtained for comparison with the simplified model based on the approximate heat transfer coefficients.

Chapter **4** presents electro-thermal parametric studies with the heatsink dimensions on co-pol, x-pol directivity, and junction temperature. Appropriate heatsink dimensions are selected for the finite array design. Scanning abilities of such both linear and planar arrays are studied. A comparitive study of the designed heatsink array and the regular patch array are made.

Chapter **5** summarizes the thesis work and gives concluding remarks and future recommendations.

2

Heatsink Antenna Design - EM Aspects

The generic goal of this chapter is to design a mm-Wave heatsink antenna which provides the electromagnetic and thermal dual functionality. The antenna is designed to resonate at a frequency of 28 GHz and its EM performance has been evaluated. To achieve this, a conventional coaxial-fed patch antenna is designed first and the heatsink is attached on top of the microstrip patch. Then, EM performance will be compared between the regular patch and the heatsink antenna. Maximum co-polarization and cross-polarization directivity will be analysed for different heatsink geometry. Based on the analysis, heatsink antenna design will be modified to have the best EM performance. The effects of different geometries and orientation of the heatsinks are studied. Two different heatsink geometries are considered: rectangular extruded fin and cylindrical fin. Finally, the coupling and scanning abilities of such heatsink antenna in a very large array is examined using infinite array analysis.

2.1. mmWave Patch Antenna Design With Heatsink On Top

Firstly, a microstrip patch antenna is designed resonating at 28 GHz frequency and then a heatsink with rectangular fins is attached on the top. Using the basic patch design equations shown below, the initial length and width were calculated and then they were tuned so that the patch resonates at 28 GHz. The initial width and length are calculated using Eq.**(2.1)-(2.4)**

$$W_p = \frac{c}{2f\sqrt{\frac{\epsilon_r+1}{2}}} \tag{2.1}$$

where W_p is the width of the patch, f is the frequency, c is speed of light in vacuum and ϵ_r is the relative permittivity of the substrate. Here, Rogers RT5880 material is used as the substrate for the patch with permittivity $\epsilon_r = 2.2$ and height $H = 0.2718mm$.

$$\frac{\Delta L}{H} = 0.412 \frac{(\epsilon_{reff} + 0.3)(\frac{W_p}{H} + 0.264)}{(\epsilon_{reff} - 0.258)(\frac{W_p}{H} + 0.8)} \tag{2.2}$$

where ϵ_{reff} is the effective dielectric permittivity given by

$$\epsilon_{reff} = \frac{\epsilon_r + 1}{2} + \frac{\epsilon_r - 1}{2}(1 + 12\frac{H}{W_p})^{-1/2} \tag{2.3}$$

$$L_p = \frac{c}{2f\sqrt{\epsilon_{reff}}} - 2\Delta L \tag{2.4}$$

The patch size is $L_p = 3.3mm$, $W_p = 4.77mm$ and it is fed by a coaxial feed beneath the groundplane which is suitable for potential 3D integration. The groundplane and patch are made of copper with $17\mu m$ thickness. The patch design and the heatsink antenna design are shown in Figure **2.1** and **2.2** respectively.

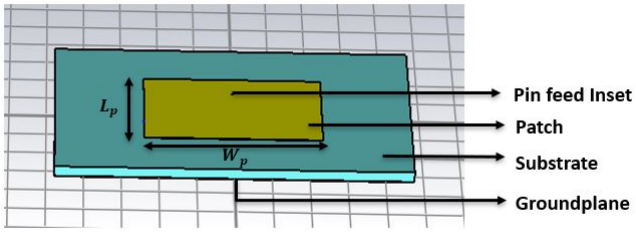

Figure 2.1: CST Model of Coaxial fed patch antenna

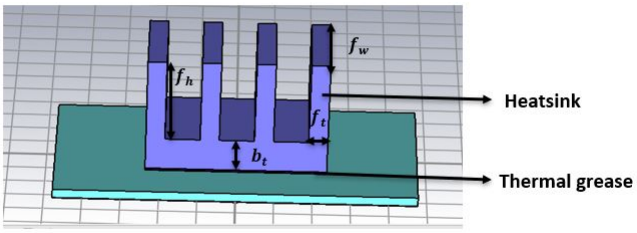

Figure 2.2: CST model of patch antenna with heatsink on top

For the heatsink antenna, the coaxial pin inset, feed pin diameter and patch length are tuned for it to resonate at 28 GHz. Here, the patch size is $L_p = 3.16mm$ and $W_p = 4.77mm$. A thermal grease material is attached between the patch and the heatsink in-order to eliminate the air gaps and maximize heat transfer to the heatsink. The thermal grease material is silicone heat transfer compound with dielectric permittivity 3.81.

Aluminium is used as the heatsink material. The heatsink base thickness, fin thickness, fin height, and fin width are marked in Figure **2.2** as b_t, f_t, f_h, f_w respectively. Here, the entire heatsink geometry is enclosed within the patch size and this is done to take care of the mutual coupling effects while designing the element in an array. Also if the heatsink geometry is extended beyond the patch length (along y), the pattern becomes distorted as seen in Appendix **A**. The fin width f_w is the same as the length of the patch $L_p = 3.16mm$, the fin height f_h is $2mm$, the fin thickness f_t is $0.5mm$, and the heatsink base thickness b_t is $1mm$. In order to make sure that the geometry of the heatsink is bounded within the size of the patch, the spacing between the fins becomes dependent on the fin thickness, number of fins, and the width of the patch if the fins of the heatsink are oriented along the width of the patch like in Figure **2.2**. The spacing can be calculated as from Eq.**2.5**

$$S = \frac{W_p - (N * f_t)}{N - 1} \tag{2.5}$$

where S is the spacing between the fins and N is the number of fins. L_p replaces W_p in Eq.**2.5** if the fins are oriented along the patch's length and in this case the fin width will be the patch width. The values of the fin dimensions considered here are based on intuition and more parametric studies on the heatsink dimensions will follow.

2.1.1. Comparison With The Regular Patch Antenna

The two antennas were designed and simulated using CST 3D electromagnetic simulation tool. The return loss shown in Figure **2.3** indicates that both the antennas resonate at 28 GHz. The co-polarization and cross-polarization pattern directivity for both patch and heatsink antenna are shown below in Figures **2.4**, and **2.5** respectively. The desired polarization is the co-polarization and the polarization that is undesirable is the cross-polarization. High cross-polarization is generally undesired as it may lead to high interference in systems using dual polarization for frequency re-use and capacity enhancement.

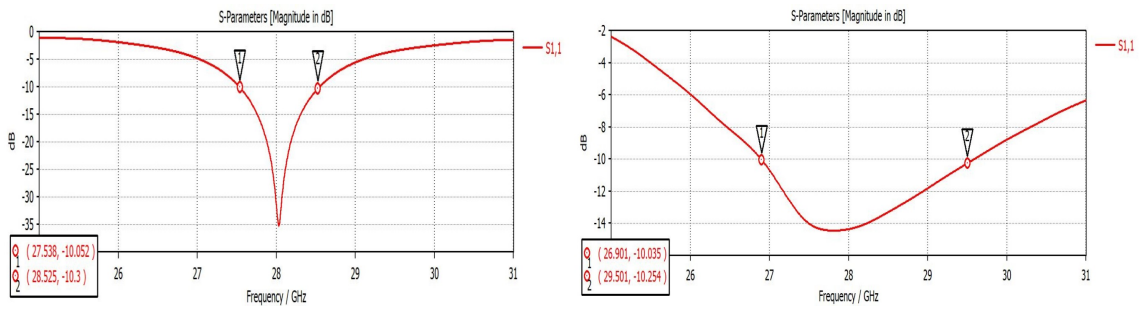

(a) (b)

Figure 2.3: Return loss S11 (dB),(a)Patch antenna,(b)Heatsink antenna

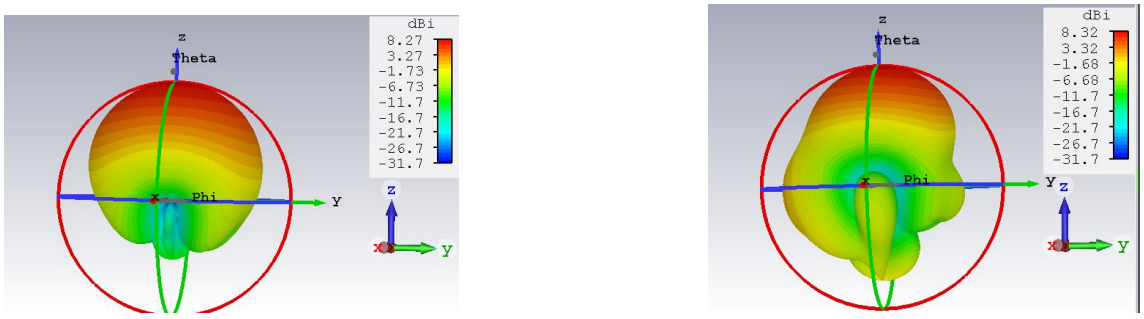

(a) (b)

Figure 2.4: Co-pol pattern directivity (dBi), (a) Patch Antenna, (b) Heatsink Antenna.

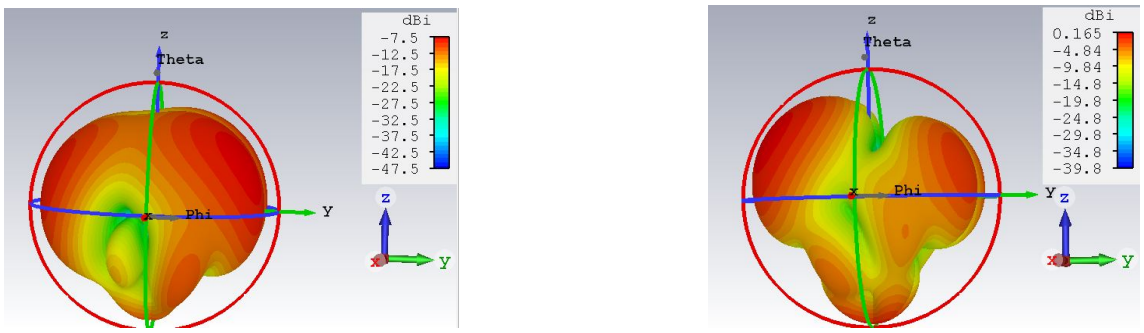

(a) (b)

Figure 2.5: Cross-pol pattern directivity (dBi), (a) Patch Antenna, (b) Heatsink Antenna.

Parameters	Patch Antenna	Patch antenna with heatsink
Resonant Frequency (GHz)	28.03	27.9
Peak Directivity (dBi)	8.273	8.307
Radiation efficiency	0.94	0.974
Peak Gain (dBi)	8.024	8.2
Realized Gain (dBi)	7.961	8.031
S11 (dB) (f=28 GHz)	-35.2	-14.44
Peak Cross-Pol Directivity (dBi)	-7.5	0.165
-10dB Impedance Bandwidth (GHZ)	0.987 (3.52%)	2.668 (9.56%)

Table 2.1: Comparison of EM performance

Table **2.1** shows the simulated EM performance comparison between patch antenna and the heatsink antenna. From Figure **2.4** and Table **2.1**, it is seen that there is a slight increase in directivity with the heatsink antenna case. The pattern directivity at broadside is similar for both the antennas but with higher back lobe for the heatsink antenna. The radiation efficieny is high for both the antennas as the substrate permittivity and the loss tangent are low. A higher ϵ_r results in tightly contained fringing fields resulting

in less radiation whereas a smaller ϵ_r results in high radiation due to loosely bound fringing fields [23]. The radiation efficiency in the case of heatsink antenna is slightly improved due to the heatsink structure. However, a large improvement on radiation efficiency with the heatsink structure is discussed in Chapter **4** with the FR-4 substrate that has high loss tangent (δ) and electrical permittivity (ϵ_r). A significant enhancement in bandwidth is observed for the heatsink antenna and this is because of more efficient use of available volume in a sphere by the 3D heatsink antenna [7].

The peak cross-polarization directivity (x-pol) is higher in case of the heatsink antenna which is undesirable, whereas the patch antenna has relatively low cross polarization level. The peak cross-polarization directivity was found to be around -7.5 dBi at ($\phi = 307°, \theta = 65°$) for the patch and 0.165 dBi at ($\phi = 305°, \theta = 62°$) for the heatsink antenna. The peak co-polarization directivity is found to be about 8.273 dBi and 8.31 dBi at $\theta = 0°$, $\phi = 0°$ to 360° for the patch and heatsink antenna respectively. As it is important to have less cross-polarization level, the effects of heatsink dimensions on both co-polarization and cross-polarization directivity will be studied in the following sections.

2.1.2. Analysis Of X-pol Directivity With Heatsink Dimension

The maximum cross-polarization level was found to be around 0.165 dBi for the heatsink antenna which is much higher than the regular patch which was -7.5 dBi. A parametric study has been made to check if the change in heatsink dimensions has impact on this maximum cross polarization level. The heatsink base thickness and fin height of the heatsink antenna are varied to see the effects on cross-pol directivity. Figure **2.6** and **2.7** shows the peak cross-polarization directivity with different fin height (f_h) and heatsink base thickness (h_b). respectively

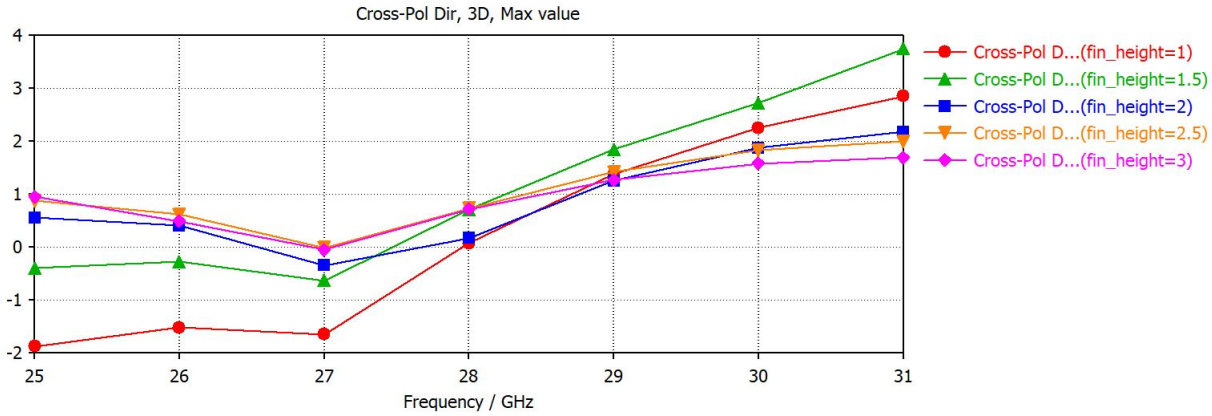

Figure 2.6: Maximum cross pol Directivity (dBi) vs Frequency

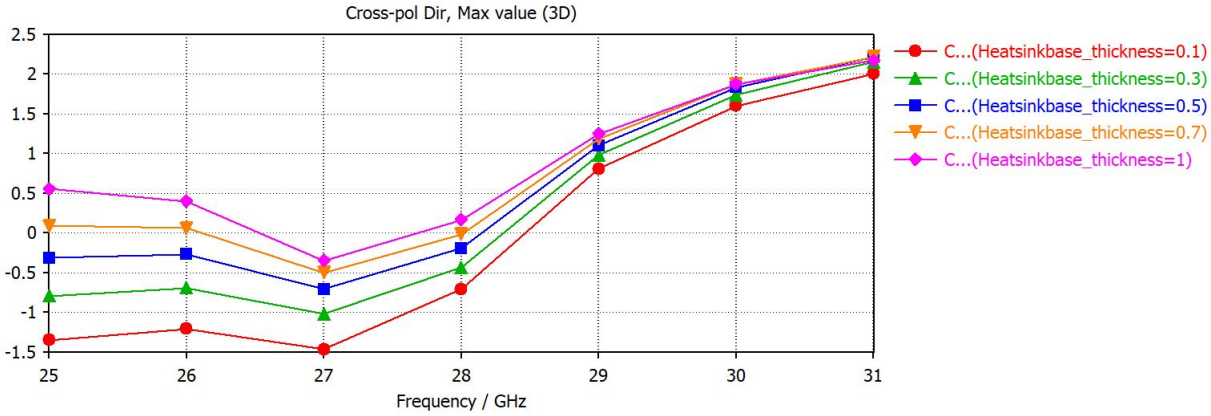

Figure 2.7: Maximum Cross-Pol Directivity (dBi) vs Frequency

The heatsink parameters $f_t = 0.5mm, h_b = 1mm, f_w = 3.16mm$ were kept constant and height of the fin was varied from $1mm$ to $3mm$. As the fin height is increased, the cross-polarization level increased to small degree. Peak cross-pol level at 28 GHz was found to be around 0.023 dBi for $f_h = 1mm$. For the analysis with the heatsink base thickness, the fin height $f_h = 2mm, f_t = 0.5mm, f_w = 3.16mm$ were kept constant and the thickness of the heatsink base was varied from $0.1mm$ to $1mm$. The behaviour of cross-polarization level was alike as in the case with fin height. The impact of base thickness on cross-pol level was slightly more than that of the fin height's impact. With less heatsink base thickness of 0.1 mm, peak cross pol directivity was found to be around -0.8 dBi.

2.1.3. Effect Of Removing Heatsink Base

The dimensions of the heatsink can be chosen such that antenna has a lower cross polarization level. Reducing the heatsink dimension has shown some improvement in lowering the cross-polarization directivity. Contrary to this, shrinking the heatsink dimension reduces it's thermal performance. As reducing the heatsink base thickness has more impact on lowering cross-polarization and also improving the co-polarization directivity, the base of the heatsink has been removed. The fins are directly placed on the top of the patch as shown in Figure **2.8** with thermal paste between them.

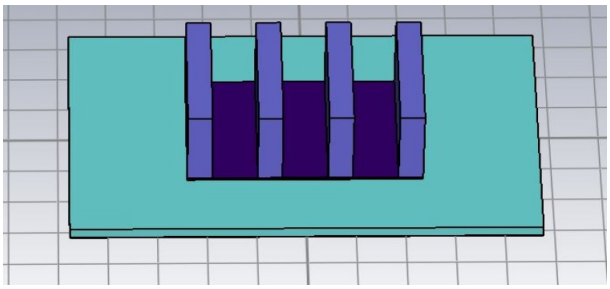

Figure 2.8: CST Model of Coaxial fed patch antenna with heat fins on top

This modified heatsink antenna design showed improvement in cross-polarization and co-polarization directivity. The peak cross-polarization directivity is found to be around -1.39 dBi at $\phi = 305°, \theta = 70°$ and the peak co-polarization directivity is found to be improved from 8.3 to 9.1 dB at $\theta = 0°$, $\phi = 0°$ to 360° and the max cross polarization level is -10.49 dB lower than the co-polarization level. The direction of maximum cross-polarization is important as it causes interference with the desired polarization direction. Low cross polarization levels close to the regular patch antenna can be achieved with change in substrate material and permittivity which will be discussed in Chapter **4**. The return loss and pattern directivity for the modified heatsink antenna are shown in Figures **2.9** and **2.10** respectively. The EM performance comparison will be discussed in the next subsection.

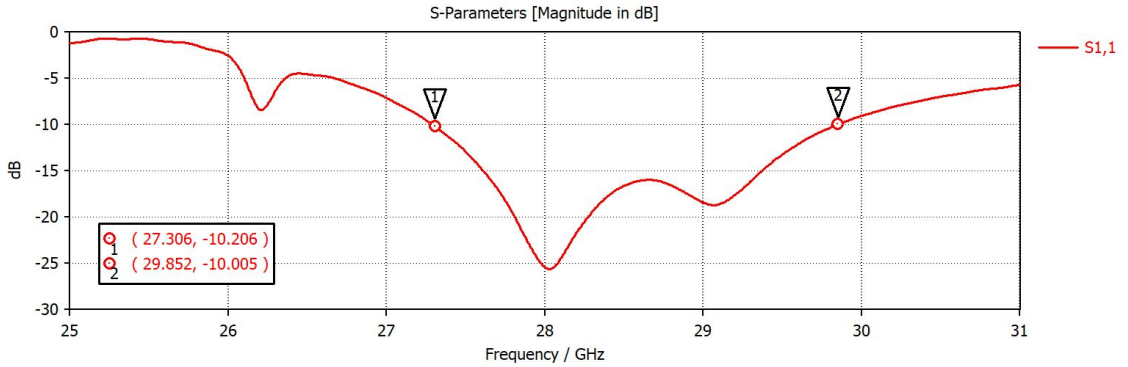

Figure 2.9: Return loss S11(dB)

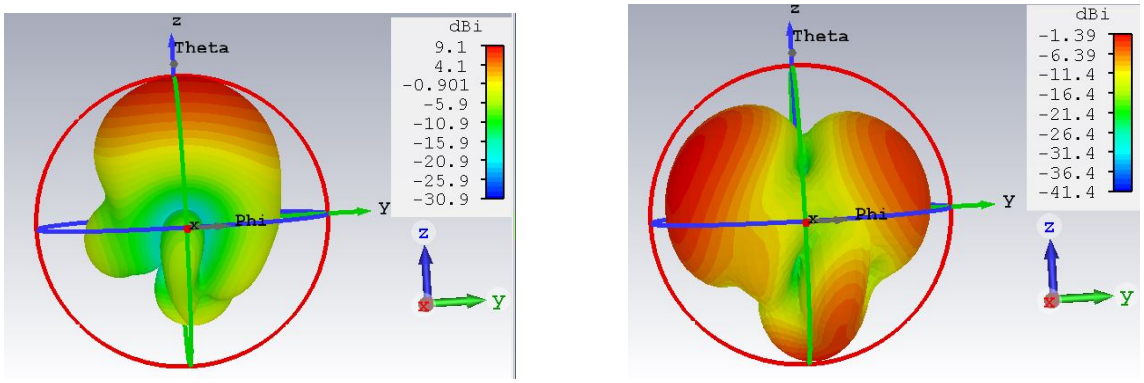

(a) (b)

Figure 2.10: Pattern Directivity for the patch with heat fins (dBi) (a) co-pol, (b) cross-pol

2.2. Effects Of Geometry And Orientation Of The Heatfins

Two different heatsink geometries are considered here: 1) Extruded rectangular fin structure 2) Cylindrical/Radial pin fin structure. Two different orientations for the rectangular fins and three different orientations for the radial pin fin case are designed and their corresponding EM performance are studied. Figure **2.11** shows the different geometry and orientation of heatsink antenna and its 3D Radiation pattern respectively.

The different orientations considered in the rectangular fin geometry are (a). Rectangular fins with fins parallel to the non-radiating edges of the patch (PNRE), (c). Rectangular fins with fins parallel to the radiating edges of the patch (PRE). The rectangular fins are aligned along the patch's length in the case of PNRE and it is aligned along the patch's width in the case of PRE.

Three different orientations are considered in the radial pin fin geometry, (e). Radial pin fins all around the top of the patch, (g). Radial pin fins across the edges of the patch, and (i). Radial pin fins near the centre of the patch. Peak directivity, peak gain and radiation efficiency of the respective heatsink antenna orientation has been tabulated in Table **2.2**

Heatsink orientation	**Peak Directivity (dBi)**	**Peak Gain (dBi)**	**Radiation Efficiency**
Rectangular fins parallel to non-radiating edges (PNRE)	9.096	8.9	0.956
Rectangular fins parallel to radiating edges (PRE)	6.234	6.16	0.983
Radial pin fins all around the top of the patch	4.918	4.73	0.962
Radial pin fins (Edges)	5.863	5.637	0.95
Radial pin fins (near the center)	9.074	8.772	0.933

Table 2.2: Comparison of EM performance for different heatsink geometries and orientations

The radiation efficiency for all the cases are above 90 % with rectangular fins (PRE) having the highest radiation efficiency of about 98.3 % indicating that it has the lowest conduction and dielectric loss.

With the fins parallel to non-radiating edges (PNRE) orientation, the peak gain is around 8.9 dBi which is 0.87 dB greater than that of the patch antenna as the broadside lobe is more focused due to the heatfin structure. Whereas, with the fins parallel to radiating edges of the patch, the peak gain is reduced to 6.16 dBi which is around 2 dB lower than the regular patch antenna. This is due to the fact that the fins in this case lie perpendicular to the current flow across the patch which lets the vertical surface currents flowing across the fins. This vertical surface currents is responsible for the radiation of side lobes in end-fire direction [7] as seen in Figure **2.11d**.

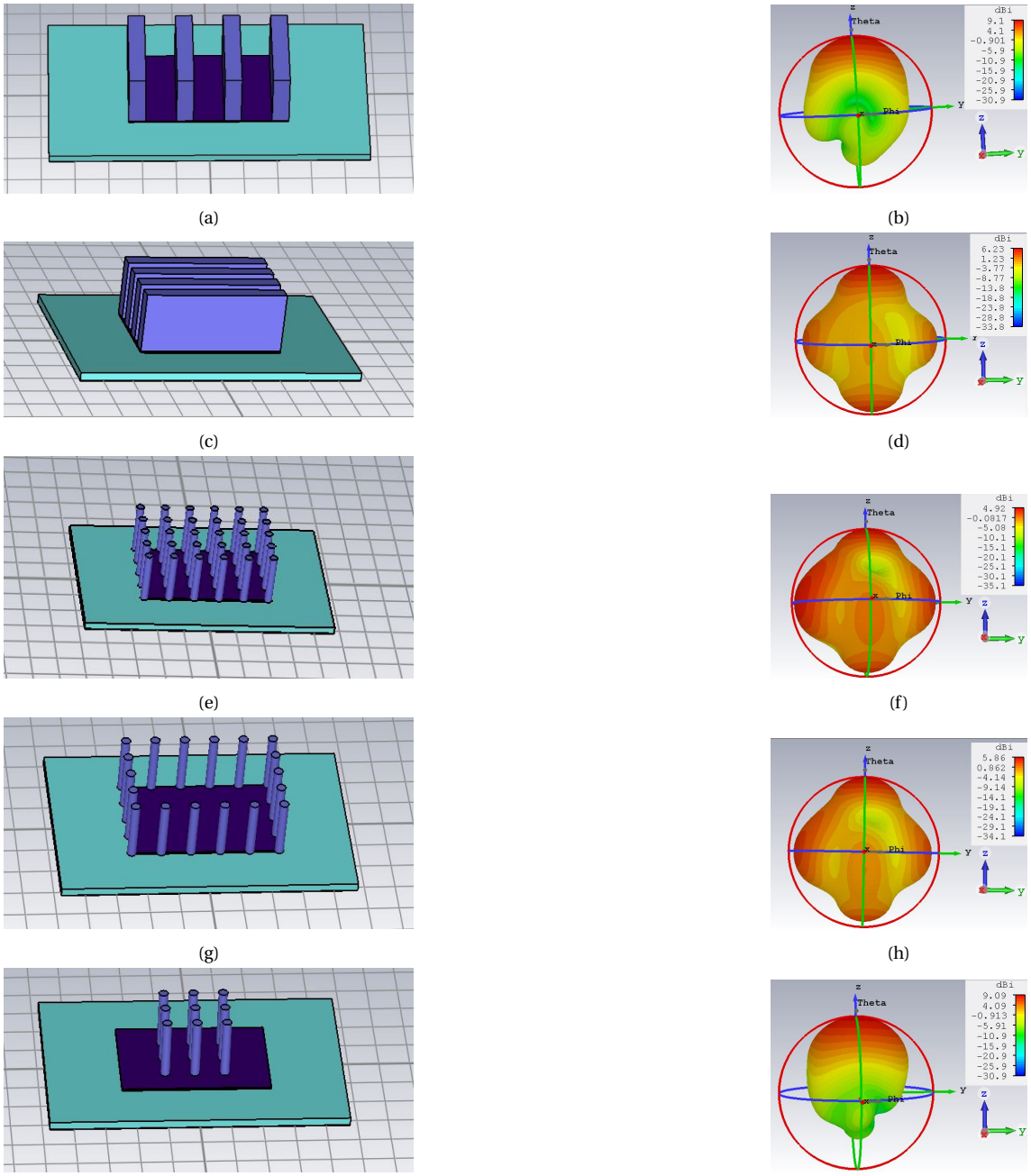

Figure 2.11: Different heatsink antenna geometry and orientations and its Radiation pattern directivity (dBi), (a,b)Rectangular fins parallel to non-radiating edges (PNRE), (c,d) Rectangular fins parallel to radiating edge (PRE), (e,f) Radial pin fins all around the top of the patch, (g,h) Radial pin fins (Edges), (i,j) Radial pin fins (near the center)

With the Radial pin fin case, the fin thickness is the diameter of the fin which is around $0.3mm$. The Radial pin fins all around the top of the patch and along the edges has lower directivity compared to the regular patch antenna. These two types have similar radiation pattern like that of the fins PRE case. But when the radial fins are placed around the center and not along the edges, the pattern has focused broadside lobe similar to that of the fins PNRE case.

Since, the rectangular fins (PNRE) and the radial fins (center) has higher directivity (focused broadside beam) than that of the regular patch antenna. These two heatfin orientations are considered for futher EM and thermal analysis. The EM performance comparison of these two orientations with the regular patch antenna is shown in Table **2.3**.

Parameters	Patch Antenna	Patch Antenna with heatsink	Patch Antenna with heat fins (PNRE)	Patch Antenna with Radial fins (centre)
Resonant Freq (GHz)	28.03	27.9	28.03	28.07
Peak Directivity (dB)	8.273	8.307	9.096	9.074
Radiation efficiency	0.94	0.974	0.956	0.934
Peak Gain (dB)	8.024	8.2	8.899	8.772
Realized Gain (dB)	7.961	8.031	8.868	8.568
S11 (dB)	-35.2	-14.44	-25.6	-16.1
Peak Cross-pol Directivity (dB)	-7.5	0.162	-1.39	-2.8
-10 dB Impedance Bandwidth (GHz)	0.987 (3.52 %)	2.668 (9.56 %)	2.56 (9.13 %)	0.694 (2.5 %)

Table 2.3: EM performance comparison of the selected heatsink orientations

2.3. Pattern Directivity With Fin Dimensions

The heatfin orientations rectangular fins PNRE and radial pin fins (center) were considered for parametric analysis with the fin parameters. Fin height, fin thickness and number of fins were varied to see the effects on pattern directivity. Figure **2.12**, **2.13**, and **2.14** shows the pattern directivity of the rectangular fin PNRE heatsink antenna with respect to different fin height, number of fins, and fin thickness respectively. Pattern directivity at constant $\phi = 0°$ and $\phi = 90°$ are shown.

Here, the initial parameters are $N = 4$, $f_h = 2mm$ and $f_t = 0.5mm$. One of the parameter is varied while the other two are kept constant considering their initial values. With the change in the fin height, directivity at constant $\phi = 90°$ is almost similar for all the cases whereas with the pattern directivity at $\phi = 0°$, back lobe increases as the fin height increases. Pattern directivity at $\phi = 90°$ is almost similar for the other parametric study as well. Except for N=3 fins, the pattern directivity at $\phi = 0°$ looks alike. Similar analaysis has been made for the radial pin fin (centre) case which is not shown here. The optimum parameters are chosen based on the maximum co-pol and cross-pol directivity which will be shown in Chapter **4**.

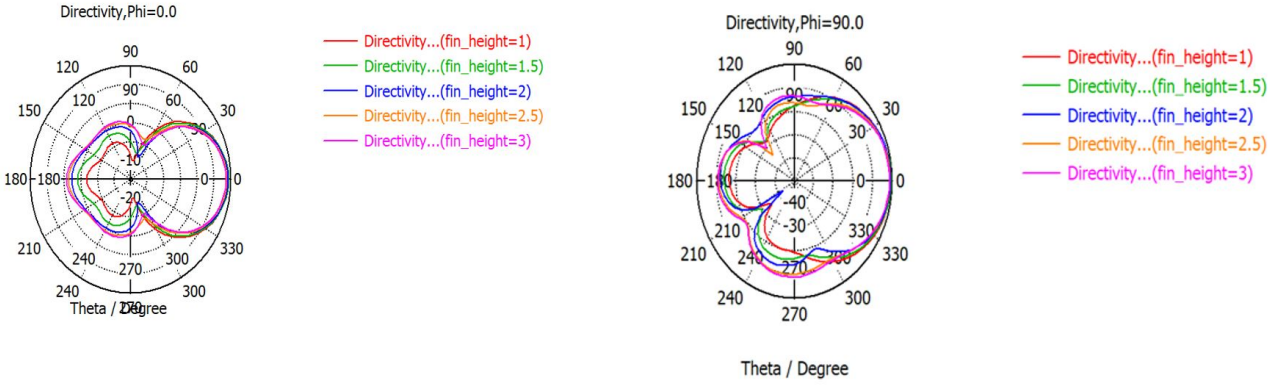

Figure 2.12: Pattern Directivity vs fin height

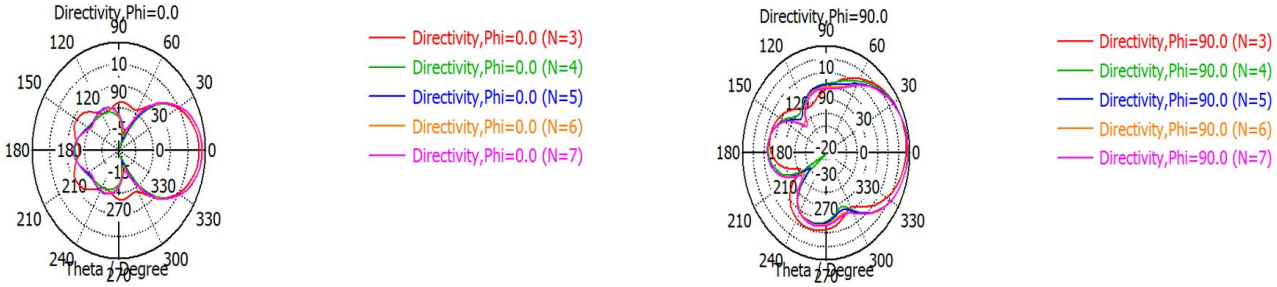

Figure 2.13: Pattern Directivity vs Number of fins

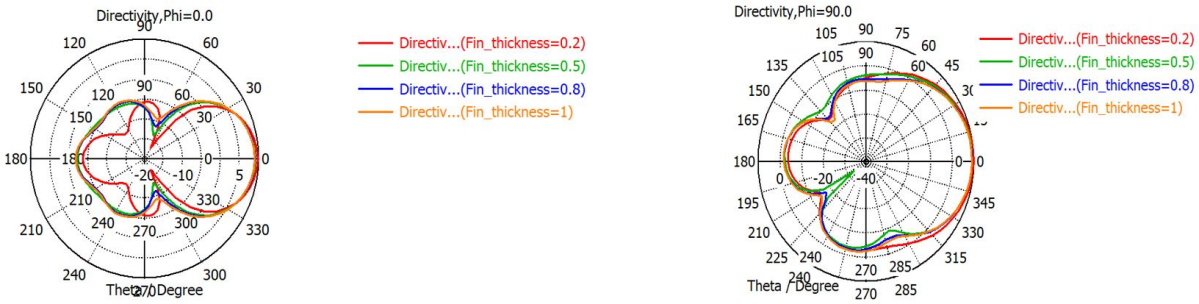

Figure 2.14: Pattern Directivity vs Fin thickness

2.4. Infinite Array Analysis Using Periodic Boundary Condition

In this section, the effects of mutual coupling between antenna elements in a very large array has been analysed. For this, an infinite antenna array approximation is

used where periodic boundary condition is applied to represent it as an infinitely extended antenna array. Using periodic Boundary conditions, mutual coupling effects can be analysed and the pattern obtained will be the embedded element pattern of the element in the infinite array. These boundary conditions will simulate a simultaneous excitation of all elements in the spatially periodic array, where the element-to-element phase shifts are given. However, the phase shift property works only with Frequency domain solver in CST, which is used in this work.

Firstly, the heatfins PNRE oriented antenna is taken and periodic boundary condition is applied on x-axis (along the width of the patch). The y-axis (along the patch length) is kept open which means that it creates infinite 1D (linear) array along x-axis. The spacing between the array elements is taken as $d_x = 0.6\lambda$. Similarly the infinitely extended array is created along y axis with $d_y = 0.6\lambda$. Figure **2.15** shows the heatfins PNRE antenna with the periodic boundary condition applied along x axis.

Figure 2.15: CST Model of heatfins PNRE array with periodic boundary condition along x axis

The return loss plots for both the infinitely extended linear arrays are shown in Figure **2.16**.

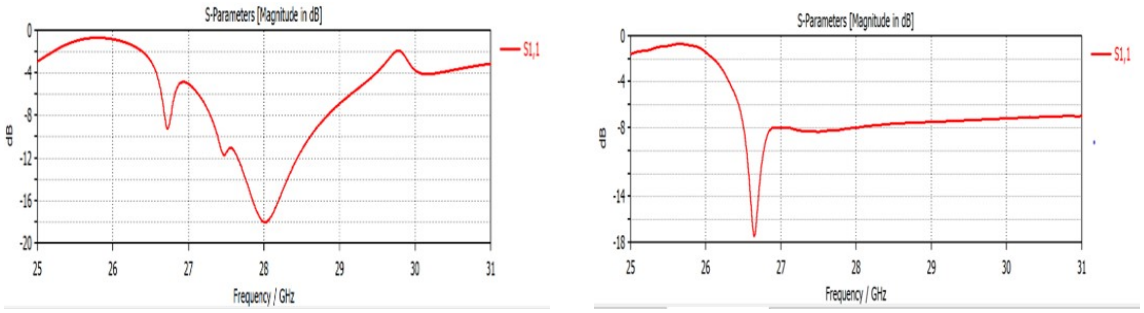

(a) (b)

Figure 2.16: Return loss S11 (dB) of infinitely extended heatfins PNRE array,(a)along x,(b)along y

It is seen that the heatfins PNRE infinitely extended along x axis has better matching at 28 GHz fequency. With the inifinitely extended array along y-axis, the resonating frequency is shifted lower to 26.7 GHz and this is due to the mutual coupling between the antenna elements. Mutual coupling along y-oriented heatsink antenna array affects the pattern and thus this heat fins (PNRE) geometry in the current form of the design is not suitable for a very large 2D array. Although the mutual coupling can be reduced by increasing the spacing between the elements, this will result in grating lobes in the

radiation pattern. The return loss plot for array infinitely extended array along y shows almost constant value of -8 dB for a wide band from 27-31 GHz (not simulated beyond 31 GHz). The S11 value can be lowered down below -10 dB to have a good matching in the wide band from 26-31 GHz by lowering the imaginary part of the input impedance. To achieve this one option could be to add lumped elements or by adding a metallic ring in the air region of the coax feed line.

A case study has been made to see the effects of inserting a metallic ring in the air region of the coax line as shown in Figure **2.17**

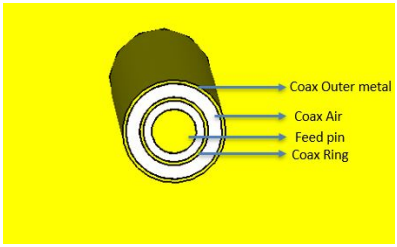

Figure 2.17: Coaxial feed with a ring inside the air region

The addition of this coax ring reduces the imaginary part of impedance and increases the real part of impedance providing good matching when it is normalized to 80Ω impedance. Figure **2.18** shows return loss properly matched having a wide bandwidth of 17.87 GHz from 26.4-44.3 GHz.

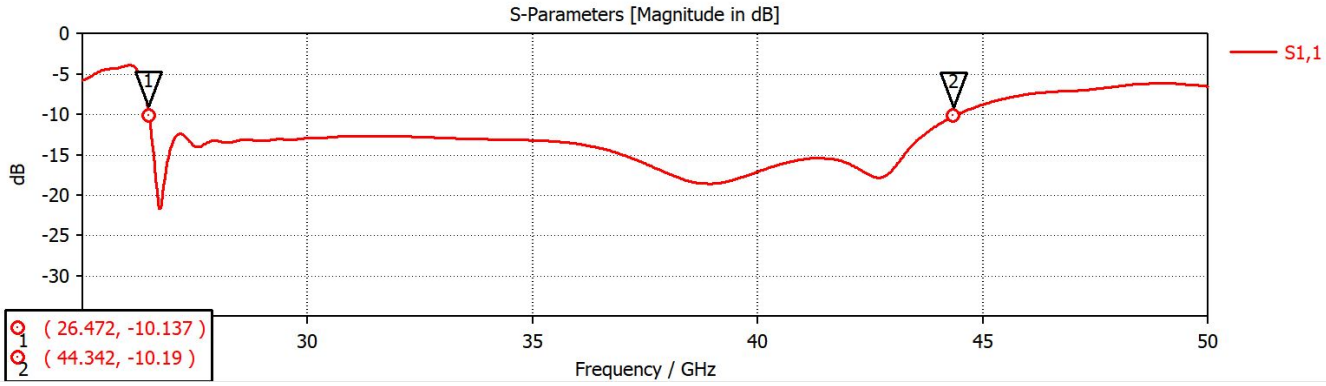

Figure 2.18: Return loss (dB)

The impedance matching effects in finite arrays are also interesting to investigate, thus this is being considered as a future research study.

Scanning range abilities can be observed by entering scan angle value in the phase shift/scan angle dialog box in CST. The heatfins PNRE infinitely extended linear array along x could achieve only ±15° scanning range. For 30° scanning and higher angles, the matching became worse. Figure **2.19** gives the return loss plot for 15° and 30° scan angle respectively. The matching is worse for 30° scan angle and this is due to the mutual coupling. This can be improved by increasing the spacing which reduces the coupling between elements.

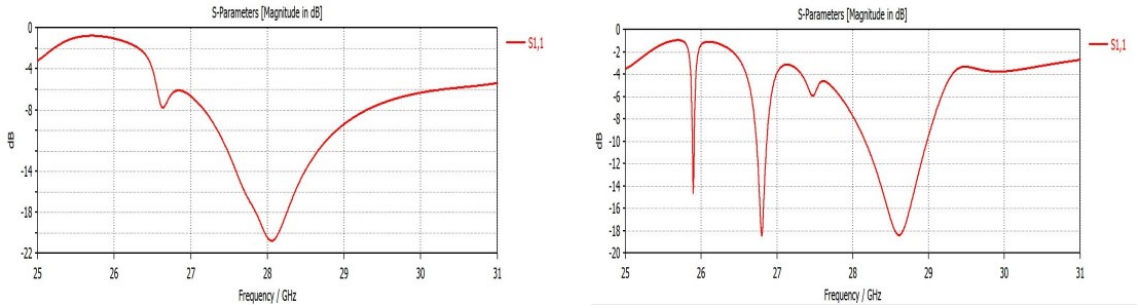

(a) (b)

Figure 2.19: Return loss S11 (dB) of infinitely extended heatfins PNRE array with scan angle,(a)15°,(b) 30°

With 15° scan angle, parametric study is made for different spacing to check the effects of mutual coupling. The spacing is varied from $d_x = 0.5\lambda$ to 1λ and the embedded pattern directivity is shown in Figure **2.20**. For $d_x = 0.5\lambda$ spacing, the pattern is distorted and this is because of mutual coupling. The pattern is also distorted at 0.9λ and 1λ which might be due to poor matching.

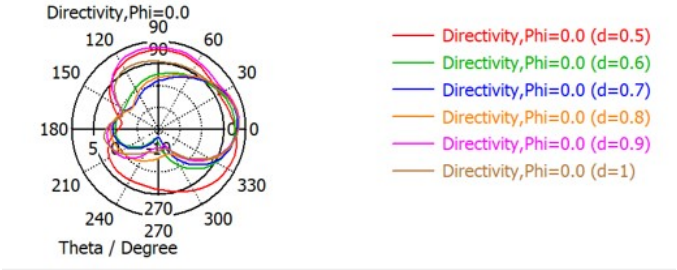

Figure 2.20: Embedded element pattern of the heat fins (PNRE) antenna with 15° scan angle

As coupling is due to the heatsink and making them close to each other increases coupling, the patch size has been reduced. Reducing the patch length reduces the width of the heat fins. The length of the patch is changed from $3.33mm$ to $2.25mm$. Shrinking the patch size and increasing the substrate permittivity makes the patch resonate along the same 28 GHz frequency. The substarte used here is FR-4 with dielectric permittivity $\epsilon_r = 4.3$. Figure **2.21** shows the embedded element pattern for the shrunk antenna. The effects of changing the permittivity and shrinking the patch size on EM and thermal aspects will be discussed further on Chapter **4**.

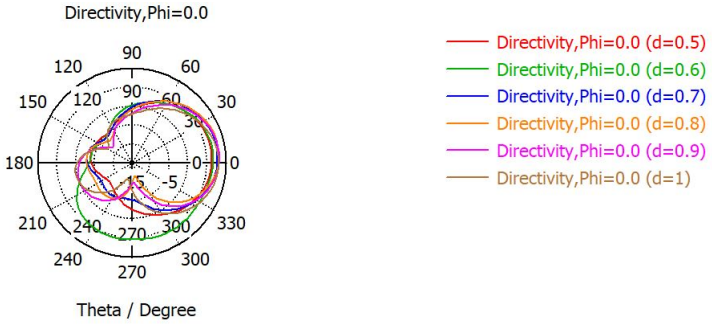

Figure 2.21: Embedded element pattern of the modified heat fins (PNRE) antenna (shrunk patch) with 15° scan angle

Similarly, the analysis is done for the radial fins (centre) orientation of the heatsink antenna. Since the variations due to the coupling effects are less significant, with x-extended and y-extended infinite arrays, periodic boundary conditions were applied across both x and y axis to form a 2D infinitely extended array. It is found to achieve about ±60° scanning range.

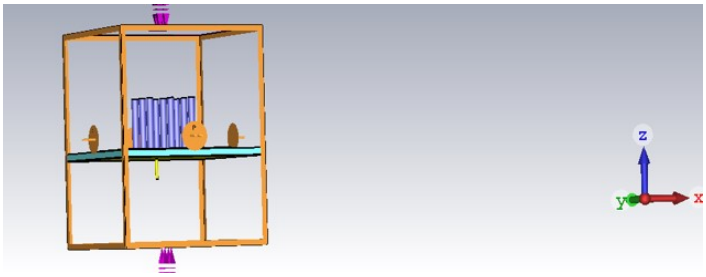

Figure 2.22: CST Model of Radial fins (centre) antenna with Periodic Boundary condition

Figure 2.23: Embedded element pattern

2.5. Conclusions - EM Aspects

In this chapter, a mm-Wave heatsink antenna element has been designed to resonate at 28 GHz frequency. The designed antenna has been modified to improve the co-pol and x-pol directivity. Among the different geometries and orientations of the heatsink antenna, rectangular fins PNRE and radial fins (center) showed preferable EM performance. The EM performance like co-pol, cross-pol directivity, realized gain, and radiation efficiencies of these two antennas are compared with that of the patch antenna.

Using periodic boundary conditions, both of these antennas are infinitely extended to see the coupling effects of such antennas in very large arrays. The x-oriented heatfins PNRE linear array is found to have a scan range of ±15° while the radial fins (center) 2D array showed a good scan range ±60°.

3

Heatsink Antenna Design - Thermal Aspects

This chapter deals with the thermal modelling and simulation of the designed mm-wave heatsink antenna integrated with an active integrated beamformer integrated circuit unit. Simulation is done with the help of two thermal models, one is a conduction based model with the assumption of convective heat transfer coefficient and the other is the air flow natural convection model without any heat transfer coefficient assumptions. Assumptions and boundary conditions for both the models are given. Junction temperature at the heat source is computed and the simulated results were compared between both the models. Effects of h.t.c, thermal resistance and radiative heat transfer on the temperature has been analysed.

3.1. Thermal Model Considerations

To model the heat flow in electronics, a standard thermal model for electronics has been used. There are two types of thermal modelling in electronic design. One is the detailed thermal model (DTMs) and the other is the compact thermal model (CTMs) [24]. Though DTMs models the IC packages more accurately, they are computationally complex. In contrast, the CTMs don't accurately model the IC packages, but they are computationally simple in predicting the junction temperature. This makes CTM more suitable for analysing heat flow problem in an efficient way [5]. Here, Two-resistor CTM is used to represent the thermal model for the designed heatsink antenna.

3.1.1. Two-resistor Model

The two resistor model as described by the JESD15-3 standard, consists of two thermal resistors connecting three nodes as shown in Figure **3.1**. The three nodes are the case node, board node and the junction node. The two resistors are junction-to-case θ_{JC} connecting the Junction and case nodes, junction-to-board resistor θ_B connecting the junction and board nodes. The junction node is where the source of the heat comes. In this case, the heat source is the beamformer chip placed on the opposite side of the antenna. The case node comes at the top of the package and the board node is the Printed Circuit Board (PCB) which is below the package's footprint.

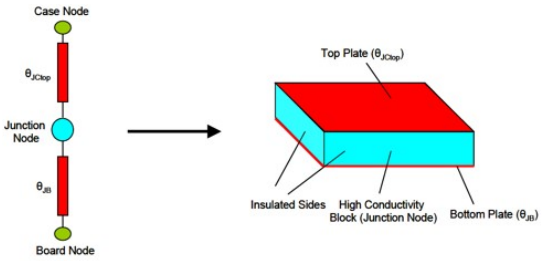

Figure 3.1: Two resistor model and its 3D space representation taken from [cite]

For simulation in 3D space, the two resistor model is represented as shown in Figure **3.1** using block and plate method where nodes are represented by block and resistors by plate. The junction block is a volume heat source and a highly conductive material. The heat flow is considered only in the normal direction. The sides are insulated to prevent leakage. The block's size is the actual size of the package and the plate's thickness and thermal conductivity can be chosen such that it obtains the actual thermal resistance value [17].

$$\theta = \frac{t}{K.A} \tag{3.1}$$

where

θ_{JC} or θ_B - thermal resistance $[K/W]$
K - thermal conductivity $[W/m.K]$
t - thickness of the plate $[m]$
A - surface area of the plate $[m^2]$

The accuracy of the two resistor model is low, but it is higher in case where most of the heat flows either through heatsink or the board [5]. An h.t.c, heat transfer coefficient value is applied at the solid-air interface to apply convective heat transfer. Heat transfer coefficient is the ratio of the heatflux to the temperature difference between the solid and surrounding fluid. At the solid-fluid regions, the thermal resistance is calculated by

$$R = \frac{1}{hA} \tag{3.2}$$

where,

R - thermal resistance at solid-fluid interface $[K/W]$
h - heat transfer coefficient $[W/m^2.K]$
A - surface area on which h.t.c acts $[m^2]$

3.1.2. Properties Of The Electronic Chip Package

The heat source here is the NXP beamformer chip attached at the back of the antenna. The 4-channel mm-Wave analog beamforming chip shown in Figure **3.2**. Amplitude and phase control in channel can be done by interfacing the chip to a computer through I2C or SPI interfaces [25]. The chip dissipates heat of about 2.3 W in Tx mode. Table **3.1** shows the parameters required for modelling the package using two-resistor model.

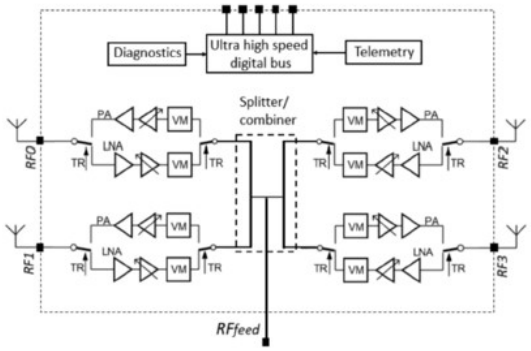

Figure 3.2: 4-channel mm-Wave NXP analog beamformer chip from [25]

Heat produced by the chip in Tx mode	$2.3W$
Chip dimensions	4.3 x 3.5 x 0.5 mm (W x L x H)
junction-to-case resistance (θ_C)	$10K/W$
junction-to-board resistance (θ_B)	$14K/W$
h.t.c at the solid-air interface	$10W/m^2K$
Ambient Temperature	$20°C$

Table 3.1: Chip parameters from [5]

3.1.3. Thermal Model Of The Antenna

Based on the NXP beamformer chip parameters, the thermal model of the antenna has been desiged using COMSOL Multiphyics simulation software. Figure **3.3** shows the thermal model of the patch antenna.

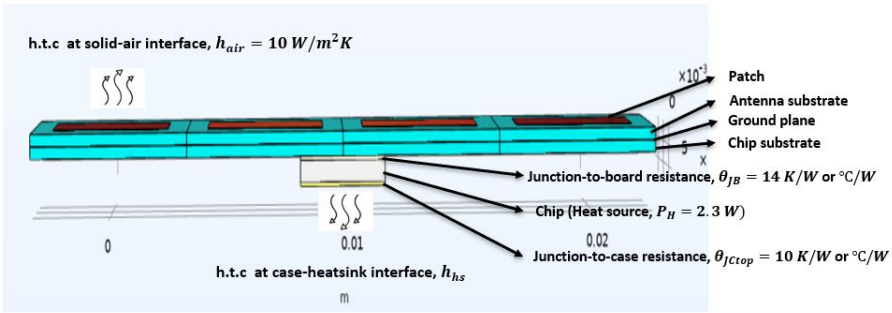

Figure 3.3: Thermal model of 4-element Linear patch antenna

As per the two resistor model representation in 3D space, the electronic chip is a highly conductive Aluminium cuboid block with the appropriate chip dimensions. The plates above and below are the junction-to-board and junction-to-case thermal resistances. From Figure **3.2**, we can see that this 4-channel analog beamformer chip is capable of

serving 4 antennas. Here, a 4-element linear patch array for single beamformer chip is designed. It can also be a 4-element 2D array depending on the heatsink geometry. The heatfins PNRE is ideal for a linear array, but the radial fins (centre) instance is suitable for a 2D array, as previously stated. For the heatsink antenna case, a thermal grease and the heat fins will be added above the patch in Figure **3.3**. Above the electronic chip are the chip substrate, ground plane, the antenna substrate and the 4 patch elements. Rogers RT 5880 material with $0.254mm$ thickness is used for both the antenna and chip substrate. Table **3.2** shows the material and thermal conductivity used for the geometries.

Geometry	**Materials**	**Thickness** (mm)	**Thermal conductivity** ($W/m.K$)
Antenna & chip substrate	Rogers RT 5870	0.254	0.2
Patch & Ground plane	Copper	0.017	400
Chip & heatsink fins	Aluminium	0.5	238
Thermal grease	Thermal grease/ thermal paste	0.05	3-8

Table 3.2: Geometry properties

For the solid-air interfaces, heat transfer coefficient value is assigned to enable convective heat flow. Above the patch, the fluid surrounding is air with ambient temperature of about $20°C$. An h.t.c value of $h_{air} = 10W/m^2K$ is assumed from $2-30W/m^2K$ which is the approximate heat transfer coefficient value for natural convection cooling regime [17]. At the bottom surface of the chip, an h.t.c value is assumed at the case-heatsink interface and this value is large from about $1000-3000W/m^2K$. The h.t.c value is supposed to be high in this case to indicate a larger heatsink at the bottom that can remove more heat via conduction or a forced convection scenario. This is done to investigate the impact of the heat transfer coefficient at the chip's bottom surface on the maximum junction temperature $T_J(°C)$. Later, instead of assuming an h.t.c value, a larger heatsink is attached at the bottom of the chip.

Now that the model is designed according to the geometry properties, the heat transfer simulation environment has to be set up. For the heat transfer simulations, COMSOL simulation environment is used.

3.2. Simulation Approaches And Boundary Conditions

Approaches used for heat transfer simulations:

- Conduction based model
- Air flow model

The assumptions and boundary conditions for these two heat transfer simulation approaches will be discussed in subsections **3.2.1** and **3.2.2**. One of the main differences between the two simulation approaches is that the conduction based model assumes

a heat transfer coefficient for a natural convective scenario, which makes the simulation easier, whereas the air flow model is based on CFD without any h.t.c assumption, making it computationally complex.

3.2.1. Conduction Based Model

Conduction is one of the three primary methods through which heat energy is transferred. It takes place by the transfer of energy within a body through small particle collisions and electron mobility. This model accounts for conductive heat transfer along with the convective cooling boundary condition, where the convective heat transfer is given by the following equation.

$$q = h.A.(T_{ext} - T) \tag{3.3}$$

where,

q - heat transferred per unit time $[W]$
h - Convective heat transfer coefficient $[W/m^2K]$
A - Area of heat transfer $[m^2]$
T_{ext} - Surface temperature of the object $[K]$
T - Fluid's temperature (air) $[K]$

Assumptions And Boundary Conditions

- The heat rate $P = 2.3W$ dissipated by the chip is applied to the heat source where the volumetric heat rate is calculated as $Q_0 = P_0/V$
- Convective heat flux is applied for all the solid regions for conductive and convective heat transfer where, the heat transfer coefficient is assumed to be $10W/m^2K$.
- The Ambient temperature is set to $293.15K$ $(20°C)$.
- Physics controlled meshing is selected with Finer meshing after checking convergence.
- Stationary study solver is used for computing the temperature field at thermal equilibrium.

3.2.2. Airflow Model

This model is based on CFD techniques, where a large cuboid box as shown in Figure **3.4** is designed enclosing the thermal model setup of the antenna in order to simulate heat transfer through natural convection. Gravity is the primary factor behind natural convection where it pulls denser fluid creating convection. The material of this cuboid box is a fluid which is air in this case.

Air flow inlet and outlet are specified in the box. The dimensions of this air box is such that it is 10 hydraulic diameter downstream (antenna to outlet), 5 hydraulic diameter

upstream (antenna to inlet) and 3-6 hydraulic diameter for the sides. In the case of fluid flow through a non-circular geometry, the hydraulic diameter is calculated by

$$D = \frac{4A}{P} \tag{3.4}$$

where,

A - Cross sectional Area $[m^2]$
P - Wetted Perimeter of the cross-section $[W/m^2K]$

For more details on calculation of hydraulic diameter and the dimensions of the air box, see Appendix **B**.

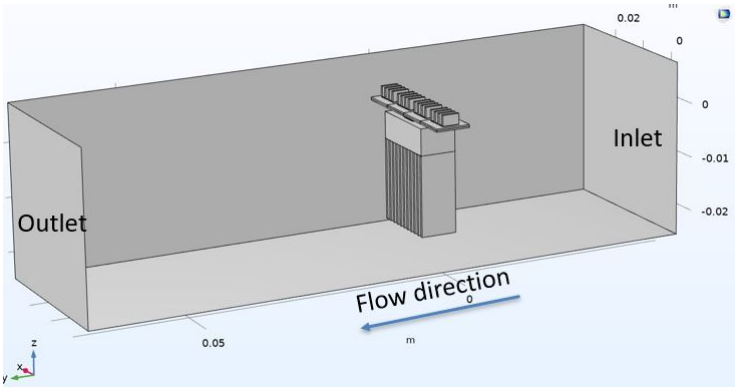

Figure 3.4: Airflow model of 4-element Linear heatsink antenna

Assumptions and Boundary conditions

- Similar to the previous model, a volumetric heat rate of 2.3 W is applied as the heat source
- For the fluid flow, a cuboid box is designed enclosing the antenna setup where the inlet and outlet domains are selected.
- The fluid is air where the thermophysical properties of air such as dynamic viscosity, thermal conductivity, density and specific heat at $20°C$ are considered.
- For the walls of the air box (except inlet and outlet boundaries), No-slip boundary condition is applied where the fluid velocity relative to the wall is zero.
- For the fluid flow, laminar flow regime is taken where a parabolic velocity profile defines the inlet velocity. The normal stress equals the outlet pressure at the outlet, and the tangential stress is cancelled.
- Gravity is enabled by the include gravity check box where it acts along +y axis (the flow direction, see Figure **3.4**) and it is equal to $9.8 m/s^2$

- A non-isothermal multiphyiscs coupling is activated which couples the fluid flow and heat transfer. Incompressible air flow is assumed, which means the fluid density remains constant during the flow. The Boussinesq approximation is selected for using non-isothermal flow with incompressible air flow assumption.
- Finer physics controlled mesh and Stationary solver are used as in the previous case

For more details on the calculations of estimate of air flow velocity, selection of fluid flow regime and boussinesq approximations, see Appendix **B**

3.3. Results And Analysis-Conduction Based Model

Simulations are carried out using the assumptions and boundary conditions mentioned above to calculate junction temperature T_J. This subsection deals with the results and analysis with the conduction based model. Both the traditional patch antenna and the heatsink antenna are compared based on the thermal aspects. As previously described, a four-element linear antenna for the heatfins PNRE oriented heatsink antenna and a four-element two-dimensional array for the radial pin fin oriented at the center are constructed, simulated, and compared to the patch antenna. At the solid-air interface, the heat transfer coefficient is $10 W/m^2K$. Figure **3.5** and **3.6** shows the Temperature plots for both the heatsink antennas compared with the patch antenna.

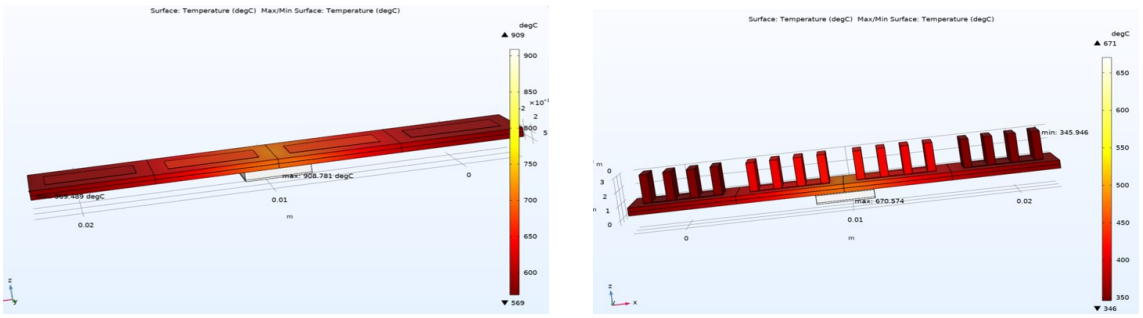

(a) (b)

Figure 3.5: Temperature plots for 4-element linear array (a) Patch ,(b)fins (PNRE) heatsink antenna

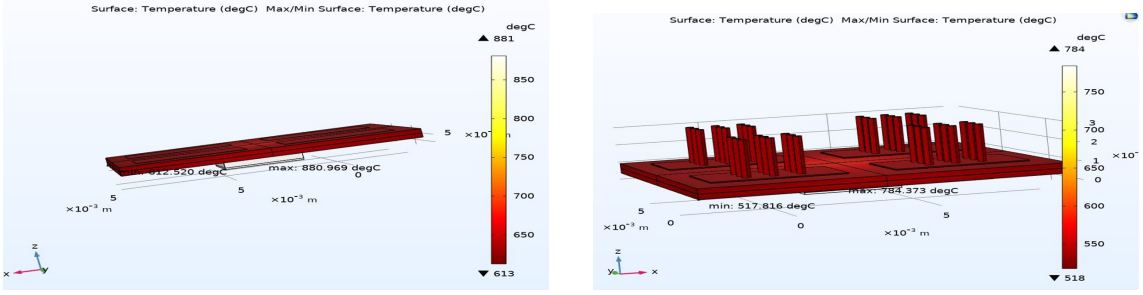

(a) (b)

Figure 3.6: Temperature plots for 4-element 2D array (a) Patch ,(b)Radial fins (center) heatsink antenna

In all the circumstances, maximum temperature is found at the heat source and the temperature is extremely high. For the linear patch array the maximum junction temperature is found to be $909°C$ and with the heatfins PNRE linear array, the maximum junction temperature is found to be $671°C$. This temperature decrease is due to the heatfins present above the patch which gives additional surface area for the heat to dissipate via conduction. Even though there is a large reduction in temperature, the components cannot withstand this high temperature. The maximum junction temperature should be maintained below $125°C$ for safe and reliable operation of the components [26]. As a result, a larger surface area is needed to remove more heat. A heatsink can be attached to the bottom of the chip to accomplish this.

3.3.1. Analysis With Different h.t.c

Rather than using a heatsink at the bottom of the chip, a higher h.t.c value is used at the bottom surface of the chip to examine how it affects the junction temperature (T_J) and antenna temperature (T_A). The temperature in the middle of the central antenna element's microstrip patch is used to calculate the antenna temperature. It is element 2 or 3 in a linear array, but any antenna element's center can be used for measurement in a 2D array since all the elements are equidistant from the chip. The h.t.c value at the bottom of the chip is varied from $1000-3000 W/m^2K$. The junction and antenna temperature plots with varying h.t.c is shown in Figure **3.7** and **3.8**

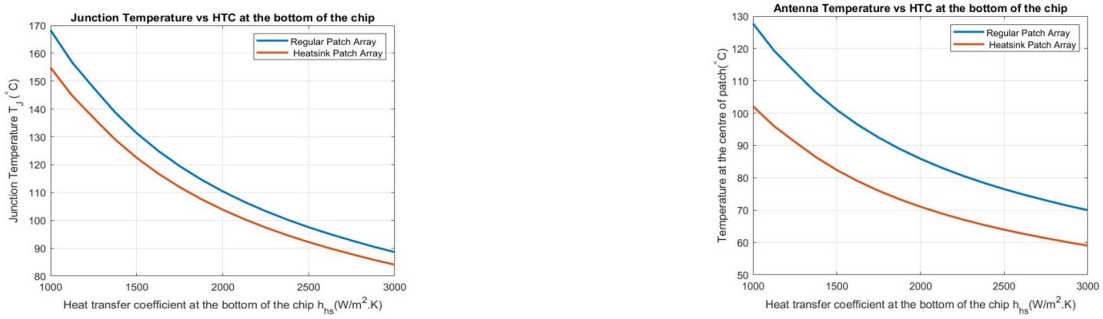

(a) (b)

Figure 3.7: 4-element linear array,(a) T_J vs h.t.c,(b) T_A vs h.t.c

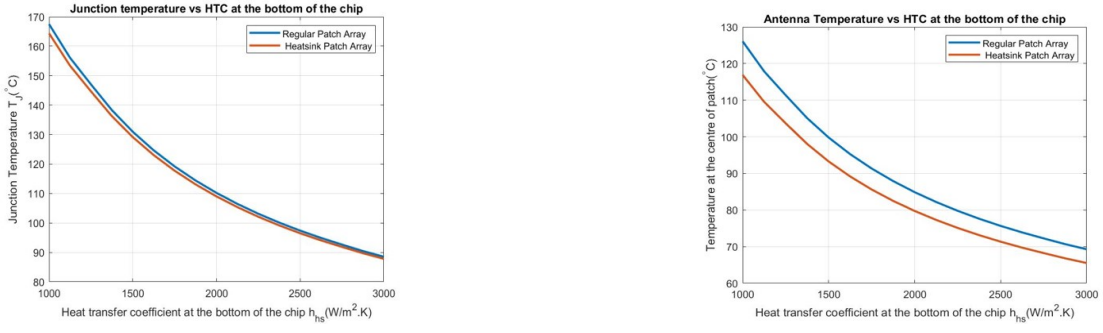

(a) (b)

Figure 3.8: 4-element 2D array,(a) T_J vs h.t.c,(b) T_A vs h.t.c

Increasing h.t.c increases heat transfer, which is evident from these plots. The patch antenna is represented by the blue line, while the heatsink antenna is represented by the orange line. The junction temperature for the linear patch and 2D patch array is determined to be $169°C$ at $1000W/m^2K$ h.t.c, whereas it is roughly $155°C$ for the heat fins PNRE antenna and $164.4°C$ for the heatsink radial fins (center) antenna. The heat fins PNRE antenna has better heat dissipation compared with the radial fins center antenna. As the h.t.c is increased further to 3000, the blue line and orange line converges for the radial pin (centre) case. This means that the heat dissipation through the radial fins is negligible when a very large heatsink structure is attached below the chip. Whereas for the rectangular fins PNRE case, the orange and blue line doesn't converge at higher h.t.c as there is always a significant difference in temperature compared to that of the patch antenna. The reason for this is due to the fact that fins PNRE heatsink antenna provides more surface area than that of the radial fins (center) heatsink antenna. There is a significant drop in antenna temperature for both the heatsink geometries when compared to the patch.

With $1000W/m^2K$ h.t.c at the bottom of the chip, the h.t.c at the antenna side is changed from $10W/m^2K$ to higher values in order to investigate the junction temperature results with a forced convection scenario (forced air from a fan). The h.t.c at the antenna side is varied from $100-300W/m^2K$ to have a forced air cooling. Figure **3.9** shows the junction temperature plot with respect to different h.t.c at the antenna side.

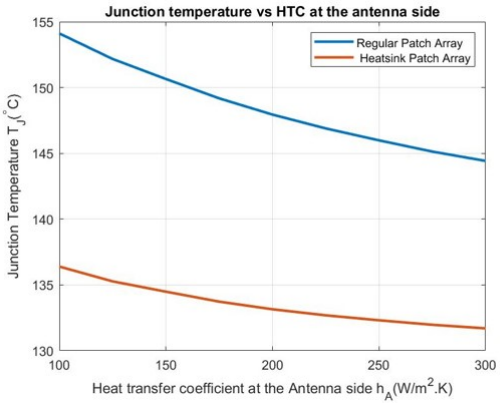

Figure 3.9: Junction Temperature vs h.t.c at the antenna side (4-element linear array)

The junction temperature of the patch reduced from $169°C$ to $154°C$ after applying $100W/m^2K$ h.t.c at the antenna side, while the temperature of the PNRE fins dropped from $155°C$ to $136°C$, increasing the temperature difference between patch and heatsink antenna. The increase in h.t.c can be attributed to the increase in velocity of the forced air which reduces the temperature even more.

3.3.2. Effects Of Chip's Parameters On Junction Temperature

To keep the junction temperature below 125 degrees, an aluminum heatsink is mounted to the bottom of the chip. The heatsink's base dimension is 4.3 x 3.5 x 0.5 mm, thickness of the fin is 0.5 mm and the fin height is about 15 mm. The simulated temperature results are seen in Figures **3.10** and **3.11**.

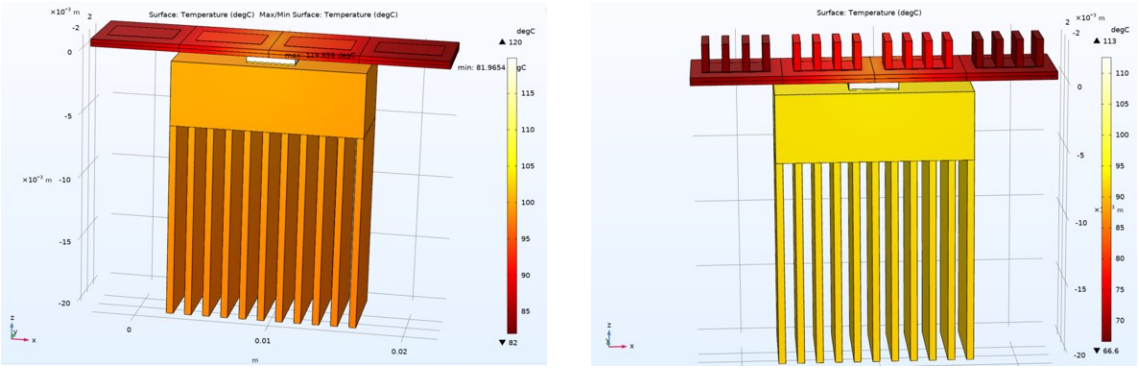

(a) (b)

Figure 3.10: Temperature plots for 4-element linear array (a) Patch ,(b)fins (PNRE) heatsink antenna

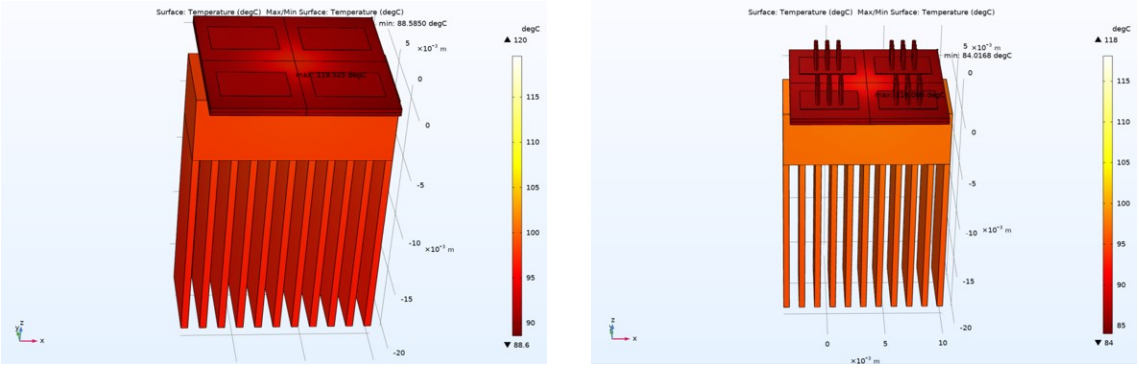

(a) (b)

Figure 3.11: Temperature plots for 4-element 2D array (a) Patch ,(b) Radial fins (center) heatsink antenna

The patch, PNRE fins, and radial fins(center) have maximum junction temperatures of 120, 112.7, and 118 degrees Celsius, respectively. Because most of the heat is transmitted via the aluminum heatsink mounted at the bottom, the temperature difference is smaller. The chip substrate and antenna substrate have a very poor thermal conductivity, which resists the flow of heat above the chip. As a result, it's critical to look at the effects of the materials used in the antenna and chip. The effects of the chip substrate and the chip's thermal resistance on the junction temperature have been researched since changing the material used for the antenna substrate will influence the electromagnetic results. From now on, only the fins PNRE case will be further investigated, as though the radial pins (center) case has good EM performance, it is not sufficient for better heat dissipation.

Material Of Chip Substrate

The chip substrate is made of Rogers RT 5880, which has a low thermal conductivity of $0.2 W/mK$ and thus inhibits heat flow above the chip. As a result, the chip substrate can be made of a highly conductive substance that can conduct more heat to the copper ground plane above the chip's substrate. Aluminium Nitride (AlN), a ceramic substrate with excellent thermal properties, is used as the new substrate material. The thermal

conductivity of AlN is about $180 W/mK$. Figure **3.12** shows the patch array and the heatfins PNRE array with AlN chip substrate.

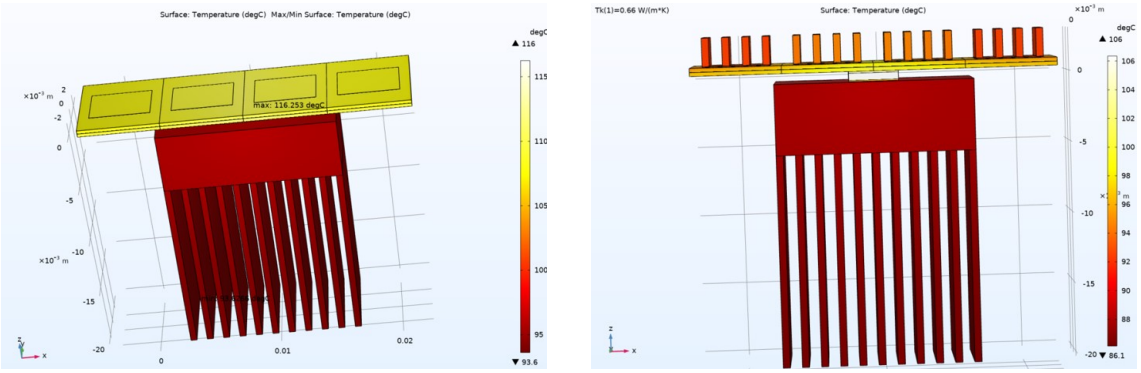

(a) (b)

Figure 3.12: Temperature plots for 4-element linear array (a) Patch ,(b)fins (PNRE) heatsink antenna

About $4°C$ temperature drop is seen with the case of regular patch and $7°C$ temperature drop is seen with the case of heatsink antenna. This enhancement is due to the AlN substrate. Further heat enhancement is possible by increasing the surface area above the antenna or by extending the copper ground plane as shown in Appendix **C**. But this has additional complexity for integration.

Effects Of Thermal Resistance

The effects of junction-to-board and junction-to-case thermal resistances on the junction temperature is studied. Figure **3.13** shows the Junction temperature varying with both the thermal resistances.

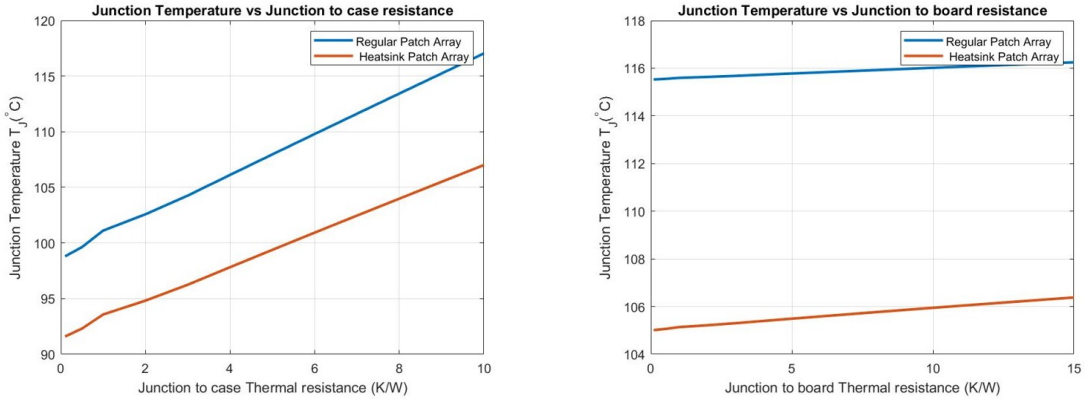

(a) (b)

Figure 3.13: Effects of thermal resistance, (a) θ_{JC} vs T_J,(b)θ_{JB} vs T_J

The thermal resistance values can be altered by altering the thermal conductivity and plate thickness. When the junction-to-case resistance is reduced, the temperature reduction is greater than when the junction-to-board resistance is reduced. This is due

to the fact that the aluminum heatsink beneath the chip provides higher surface area for heat to dissipate.

3.3.3. Radiative Heat Transfer

Apart from conduction and convection, heat is also dissipated by thermal radiation, which is carried out in the form of electromagnetic waves. Unlike black bodies, which emit all thermal radiation, other surfaces that are not perfect black bodies have an emissivity factor that determines how much heat they radiate. The thermal radiation emitted by a Gray body is given by

$$P = \epsilon \sigma A T^4 \tag{3.5}$$

where,

P - heat transferred per unit time $[W]$
ϵ - surface emissivity
σ - Stefan-Boltzman constant = 6.67x10^{-8} $[Wm^{-2}K^{-4}]$
A - radiating area $[m^2]$
T - temperature of the body$[K]$

Surface-to-Surface radiation physics is added to the existing model in COMSOL where the radiating surfaces and direction are selected. Gray body radiation node is selected and surface emissivity (ϵ) is taken from the material properties. Figure **3.14** shows the patch and heatsink antenna after radiative heat transfer has been added. In both circumstances, a temperature reduction of about 2°C is seen.

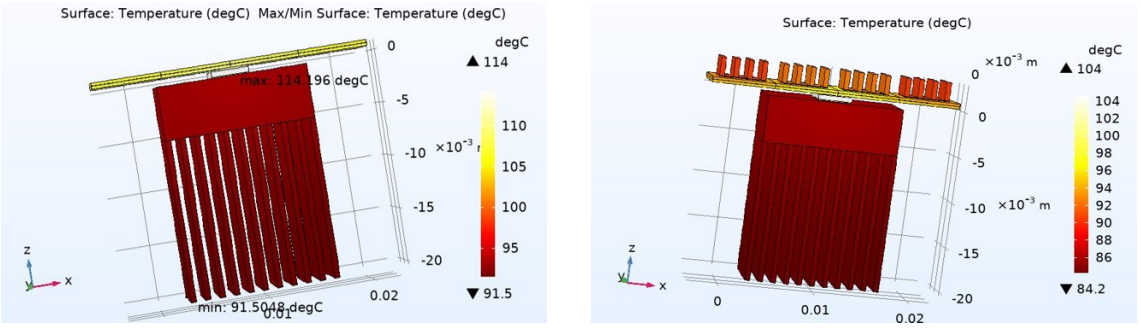

(a) (b)

Figure 3.14: Temperature plot with radiative heat transfer,(a)Patch,(b)Heatsink

Thermal radiation is directly proportional to temperature and emissivity. The materials used here have a low emissivity, particularly the polished aluminum, which has a surface emissivity of 0.05. Increasing the emissivity of the materials used is one technique to improve heat transmission by radiation. The emissivity of the aluminum heatsink can be increased up to 0.85 by anodizing it [27]. Anodizing, on the other hand, has an effect on the electrical characteristics of aluminum. Figure **3.15** shows the temperature plot of the heatsink antenna with anodized aluminium for the antenna and the heatsink placed at the bottom of the chip. The temperature reduced from 104°C to 94.2°C after using anodized aluminium.

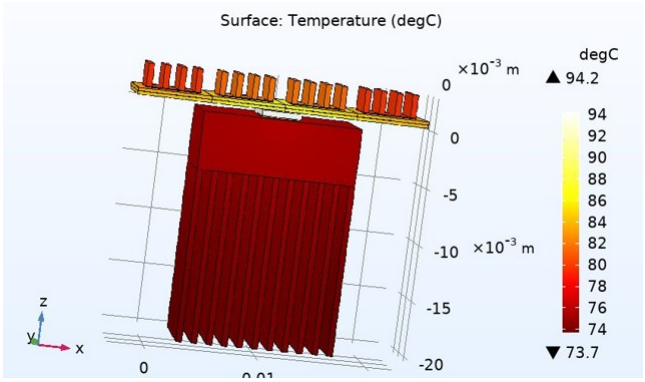

Figure 3.15: Temperature plot with radiative heat transfer using Anodized Aluminium

3.4. Results And Analysis-Airflow Model

Based on the simulation settings discussed in section **3.2.2**, temperature and velocity plots are obtained after simulation. Figure **3.16** and **3.17** shows temperature and velocity distribution for the linear patch antenna array and the heatsink antenna array respectively.

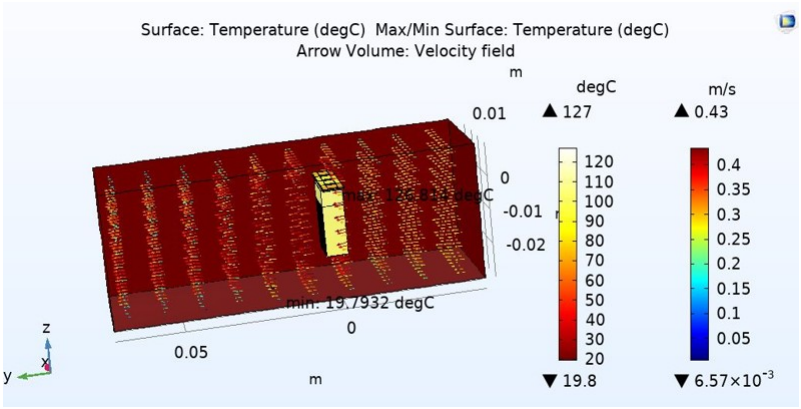

Figure 3.16: Natural convection of 4-element Linear patch antenna

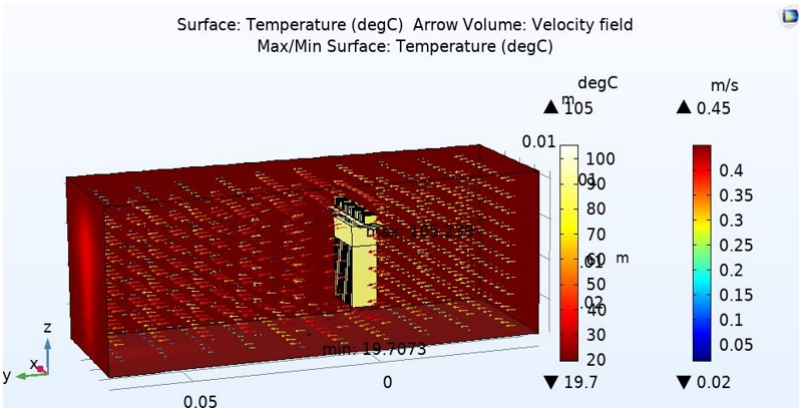

Figure 3.17: Natural convection of 4-element Linear heatfins (PNRE) antenna

Thermal Model	4-element patch antenna array	4-element heatsink PNRE antenna array
Conduction Based	114.19°C	104.05°C
Air flow	126.82°C	105.23°C

Table 3.3: Comparison of the two heat transfer simulation models

The temperature plots show that using a heatsink antenna array lowers the junction temperature by 21.6°C compared to the patch antenna. Table **3.3** shows the simulated junction temperature values based on both the models. While the junction temperature obtained is almost the same for both the models in the case of the heatsink antenna array, it is not the same in the patch antenna case. This is due to the fact that the air flow model does not assume any heat transfer coefficient because the h.t.c is unknown in most cases. Many factors influence the heat transfer coefficient, including geometry, fluid temperature, and other thermophysical parameters like as viscosity and thermal conductivity. In the case of patch antenna geometry the h.t.c will be lower when you compare to the heatsink antenna geometry and this can be also explained with the change in velocity. For heatsink antenna the typical velocity was about 0.455 m/s and for the patch antenna it came about 0.429 m/s. This velocity here is calculated at specific points selected in (x,y,z) plane. For more details on the estimate of air velocity and fluid flow see Appendix **B**.

3.5. Conclusions-Thermal Aspects

To summarize, this chapter introduces a two-resistor thermal model for electronics that includes the proper beamformer chip parameters. Two simulation methods are considered: 1) conduction with convective cooling boundary condition and 2) natural convective laminar air flow model. The heatsink antenna's simulated temperature plots are compared to the patch antenna's. Heat fins PNRE antenna dissipated heat more effectively than radial fins (center) and patch antennas.The effects of thermal resistance and the chip's material on the junction temperature is studied where lowering the junction-to-case resistance resulted in a substantial temperature drop while compared to lowering the junction-to-board resistance. The temperature dropped by roughly 4 degrees when the chip substrate was changed from a low thermally conductive Rogers RT5880 to a highly thermally conductive Aluminium Nitride. In the case of the heatsink antenna array, the junction temperature achieved is about the same for both models, but not in the case of the patch antenna. This is owing to the fact that the h.t.c for patch antenna geometry might be smaller than the assumed $10 W/m^2K$ h.t.c value, which can also be explained by the velocity change. The heatsink antenna's junction temperature is reduced by 10°C in the conduction model, while the air flow model shows a 21.6°C degree reduction in comparison to the patch antenna.

4

Heatsink Antenna - Electro-Thermal Co-Design

This chapter begins with parametric analyses of antenna dimensions and design selection based on performance in both EM and thermal aspects. The sample array implementation is then shown where scanning abilities, side lobe level and junction temperature of both patch and heatsink antenna arrays are compared. Finally, a comparison of electro-thermal performance between patch array and heatsink antenna array is made where, heatsink antenna provides a better joint electro-thermal performance trade-off.

4.1. Parametric Study With Fin Dimensions

4-element fins PNRE heatsink antenna array is considered with the heatsink attached at the bottom surface of the chip as discussed in section **3.3.2**. Keeping all the other dimensions and materials constant as discussed earlier, the fin's dimensions, such as fin height, thickness, and number of fins are modified to examine how they affect thermal and electromagnetic aspects. It's crucial to compare and contrast the EM and thermal results because this will aid in the design of a heatsink antenna with the best fin dimensions. The effects of fin dimensions on pattern shape were already examined in section **2.3** of Chapter **2**. The maximal co-pol and cross-pol directivity in relation to various fin dimensions is now being researched. As the surface area above the antenna varies due to the change in fin dimensions, the junction temperature changes. The surface area is calculated as the fin area above the patch antenna multiplied by the number of fins. The fin area here is the area of the cuboid above the patch and it is given by

$$S = 2 * (f_h * f_w + f_h * f_t) + f_w * f_t \tag{4.1}$$

$$S_{tot} = N * S \tag{4.2}$$

where,

S - Fin area $[mm^2]$
f_h - Fin height $[mm]$

f_t -Fin thickness $[mm]$
f_w - Fin width $[mm]$
S_{tot} - Total surface area above the patch $[mm^2]$
N - Number of fins

For various heatsink dimensions, co-pol directivity, cross-pol directivity, and junction temperature are investigated. The EM parameters are calculated after the designed antennas have been properly matched. These results will help in the selection of the best fin dimensions for the design.

Fin Height

The fin height is varied from 1mm to 4mm while the number of fins is kept at 4 and the fin thickness is kept at 0.5 mm. Both the conduction-based and the air flow models are simulated to evaluate the junction temperature. Figures **4.1**, **4.2** gives the junction temperature values based on conduction model and air flow model respectively.

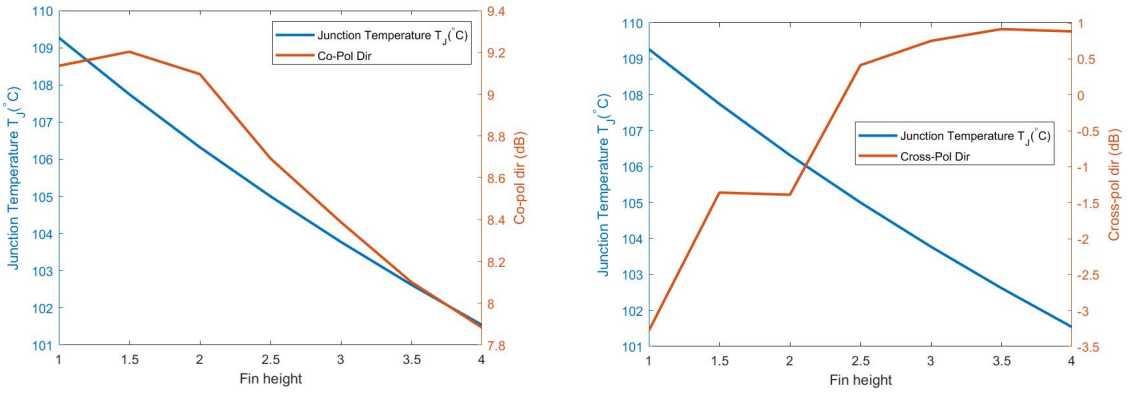

(a) (b)

Figure 4.1: Conduction Based model-Fin height vs (a)Co-pol,(b)Cross-pol

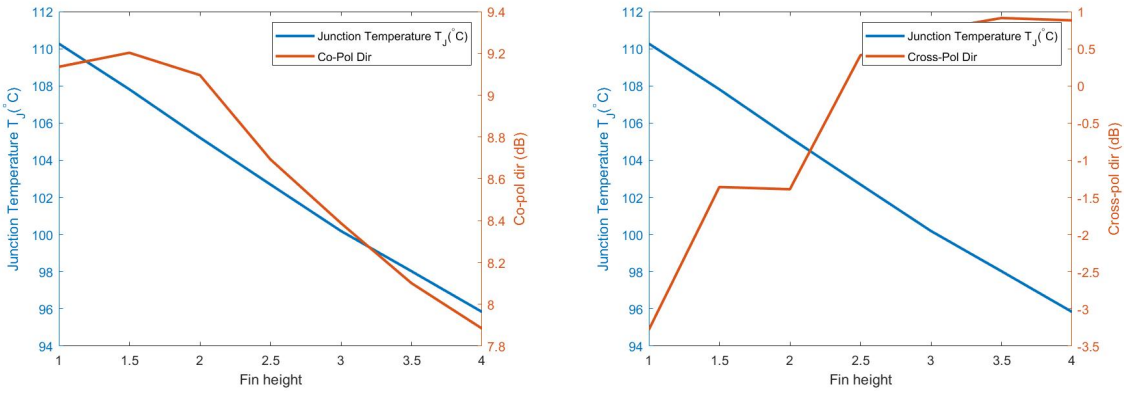

(a) (b)

Figure 4.2: Air flow Model - Fin height vs (a)Co-pol,(b)Cross-pol

When the fin height was varied from 1 to 1.5 mm, the co-pol directivity increased at first, but then declined as the fin height was increased further. However, the cross-pol directivity increased as the fin height is increased. For better performance, high co-pol and low cross-pol directivity are desirable. Both can be achieved by having reduced fin height for the heatfins, but the junction temperature will be high. Increase in fin height increases the surface area thereby reducing the surface temperature. This leads to a trade-off between EM and thermal performance. The junction temperature drops even more with the increase in fin height in the air flow model, which could be related to the geometry-induced increase in h.t.c. Based on the foregoing findings, a fin height of 2mm would be ideal, since it has a good balance of EM and thermal performance.

Fin Thickness

Here, the fin thickness is changed from 0.2 mm to 1 mm , keeping $f_h = 2mm$ and $N = 4$. Figures **4.3**, **4.4** gives the junction temperature values based on conduction model and air flow model respectively.

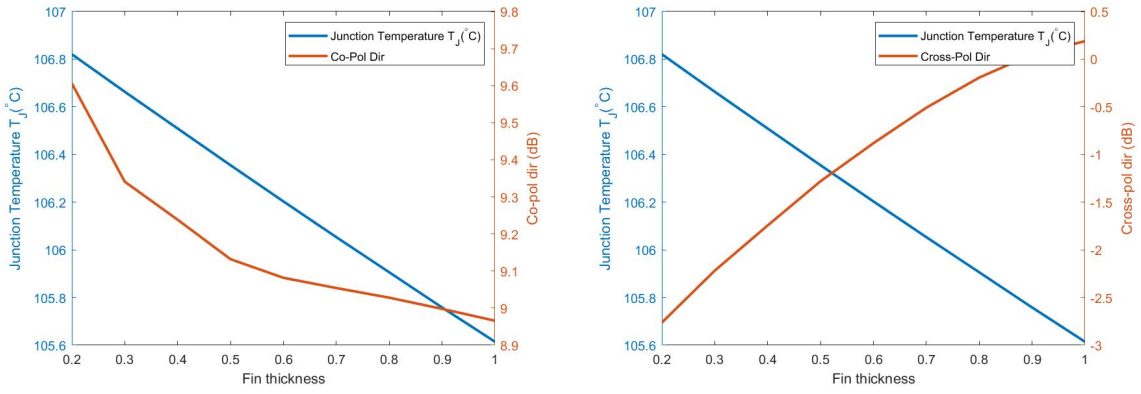

(a) (b)

Figure 4.3: Conduction Based model-Fin thickness vs (a)Co-pol,(b)Cross-pol

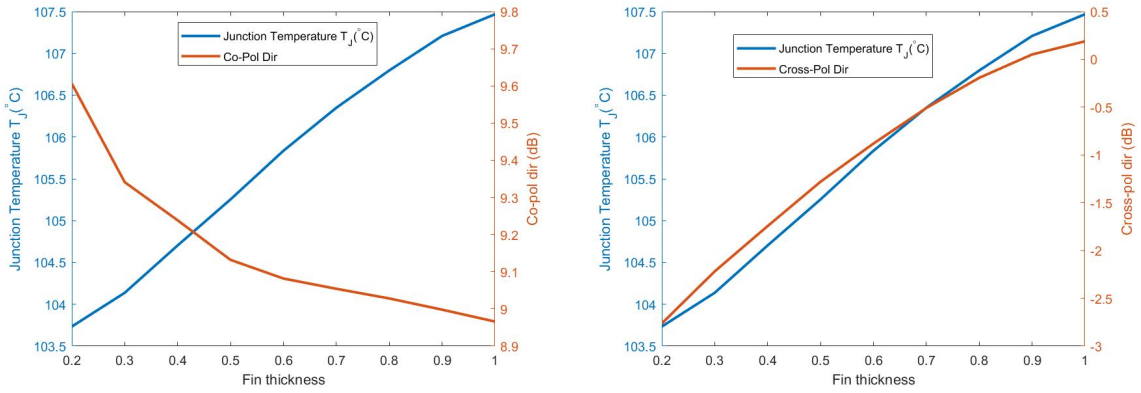

(a) (b)

Figure 4.4: Airflow model-Fin thickness vs (a)Co-pol,(b)Cross-pol

Figure **4.3** follows the same trend as with the fin height. However, as shown in Figure **4.4**, the findings of the air flow model showed an increase in junction temperature as fin thickness increased. The junction temperature rises despite the fact that the surface area increases slightly. This is because the h.t.c is also determined by the fin spacing. The greater the spacing, the greater the air flow, which results in an increase in convective heat transfer [28]. The spacing between the fins reduces as the fin thickness or number of fins increases, according to Eq.**(2.5)**. As a result, increased fin thickness leads to reduced fin spacing, resulting in a lower h.t.c.

Number of fins

Figures **4.5** and **4.6** shows the results based on Conduction and Air flow model respectively.

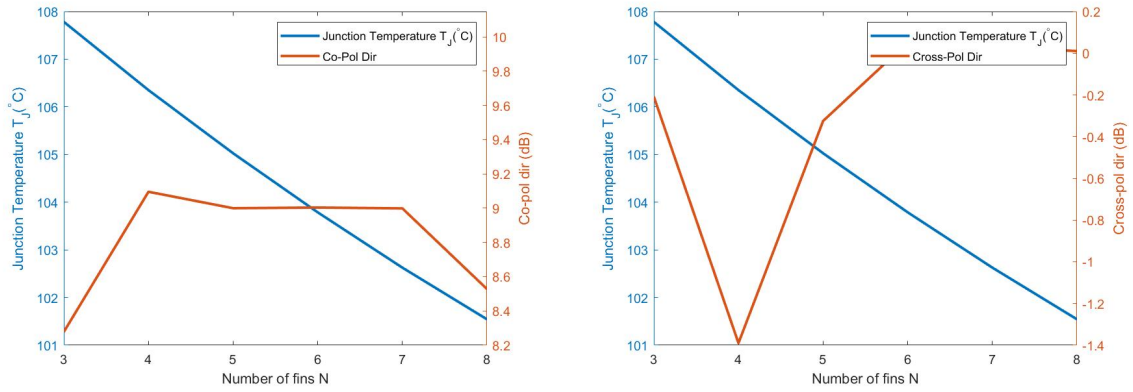

(a) (b)

Figure 4.5: Conduction Based model-Number of fins vs (a)Co-pol,(b)Cross-pol

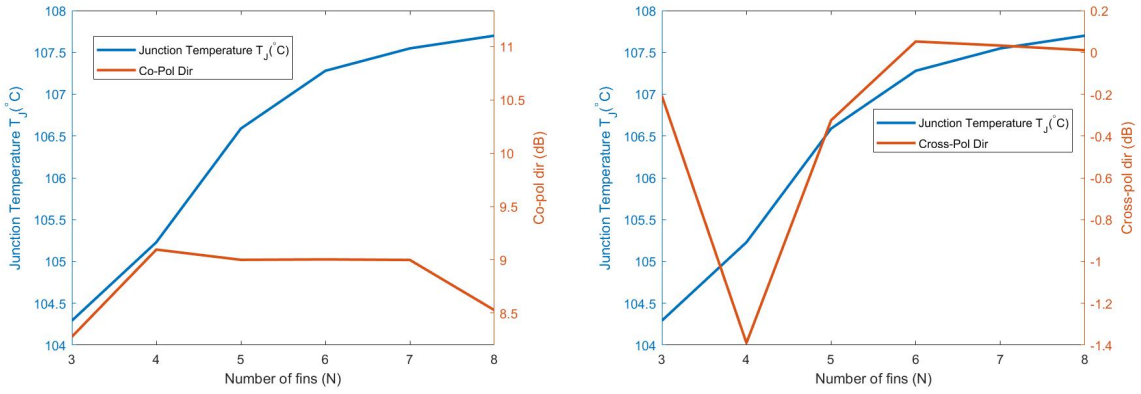

(a) (b)

Figure 4.6: Airflow model-Number of fins vs (a)Co-pol,(b)Cross-pol

The number of fins varies from 3 to 8, while the fin height and thickness remain stable at 2mm and 0.5mm, respectively. With N=4 fins, the co-pol directivity is highest and

the cross-pol directivity is lowest. The surface area increases as the number of fins increases, but the spacing reduces, reducing h.t.c. As a result, ideal number of fins would be 4. Additional parametric studies with different fin dimensions can be seen in Table **D.1** in Appendix **D**, where one can observe that the conduction based model shows a reduce in junction temperature for increase in surface area (increase in fin dimensions), whereas the airflow model takes in to account the spacing and its effects on h.t.c as previously stated.

4.2. Finite Array Implementation

In this part, a finite array heatsink antenna is developed and compared to the patch antenna, which serves as the benchmark, in terms of realized gain, junction temperature, and side lobe level. The scanning abilities of the heatsink antenna have been investigated for both linear and planar arrays. The array with 0.5λ spacing produced pattern distortion because the heatsink antenna elements are relatively close to each other, as explained in Chapter **2**. In order to construct the array with standard spacing of 0.5λ, the patch size is reduced and FR-4 substrate with $\epsilon_r = 4.3$ is used. The thermal conductivity of the FR-4 and Rogers RT5880 are comparable.

Since the permittivity of the FR-4 substrate and the loss tangent are high, fringing fields are tightly contained resulting in low radiation efficiency . For the patch antenna the efficiency is about 66.2% and for the heatsink antenna, the efficiency is improved to 80.6% because the electric field is less confined in the substrate, the surrounding medium has a greater influence on the effective dielectric constant [7]. Also, the change in the substrate had significant effect on the co-pol and cross-pol directivity. The co-pol directivity of the heatsink antenna is reduced from 9.096 to 7.4 dBi and the x-pol directivity is reduced from -1.39 to -6.06 dBi. The fin dimensions are chosen as $N = 4$, $f_h = 2mm$, and $f_t = 0.2mm$ based on the results obtained in the previous section assuming that a similar trend holds for this case with the change in substrate.

4.2.1. Linear Array Implementation

Both x-oriented and y-oriented 8-element linear heatsink antenna array with 0.5λ spacing are constructed. As previously stated, the patch antenna is used as a bench mark. Simultaneous excitation is used where all the ports/sources are excited simultaneously according to the excitation list settings.

X-oriented Linear Array

The array design, return loss and the 3D pattern realized gain plots for both the patch array and heatsink array are shown in Figures **4.7**, **4.8**, and **4.9** respectively.

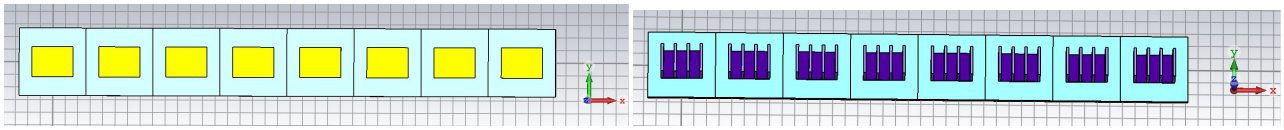

(a) (b)

Figure 4.7: Array Topology, (a) 1 x 8 Patch, (b) 1 x 8 heatsink antenna

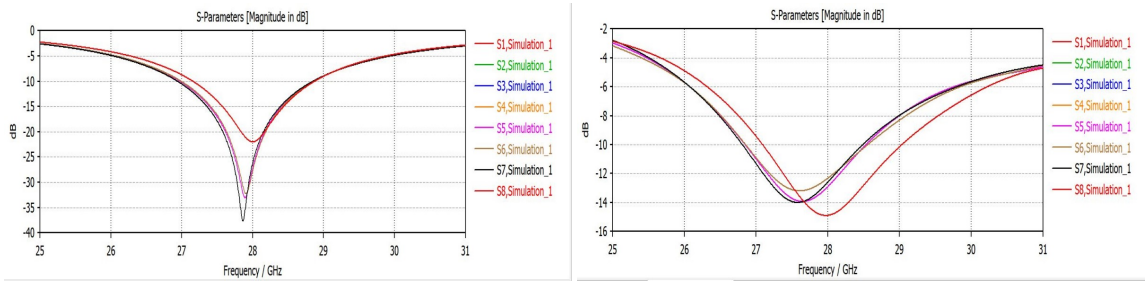

(a) (b)

Figure 4.8: Return loss S11 (dB) of 1 x 8 array,(a)Patch,(b)Heatsink antenna

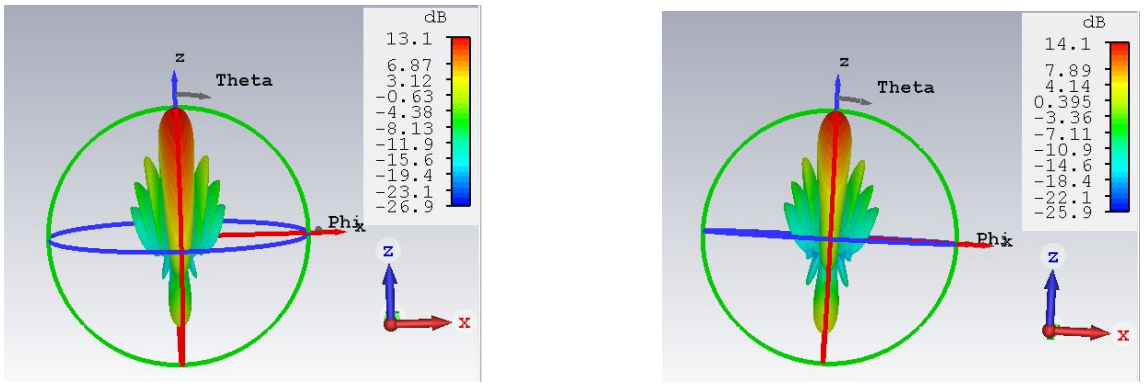

(a) (b)

Figure 4.9: Realized gain (dB), (a) Patch, (b) heatsink antenna

In comparison to the patch, the heatsink antenna array provides a higher realized gain and more surface area for heat removal. The thermal model will have two heat sources with the 8-element array, and the temperature results will be comparable to those produced with the 4-element linear array.

Both the arrays have a side lobe level (SLL) of roughly -13.5 dB. Using the Taylor or Chebyshev window, amplitude tapering can be used to further minimize the side lobe. The amplitude values for side lobe suppression for 20 and 30 dB are obtained using Chebyshev windowing. The amplitude values can be seen in Appendix **E**. Figure **4.10** shows the farfield realized gain ($\phi = 0°$) cut for the designed array. As the amplitude tapering is introduced, we can see the reduction in Side Lobe Levels but the main lobe becomes wider making the power spread over larger angle i.e. beamwidth becomes greater which results in less directivity. Table **4.1** shows the performance of the x-oriented array in terms of realized gain, SLL and junction temperature.

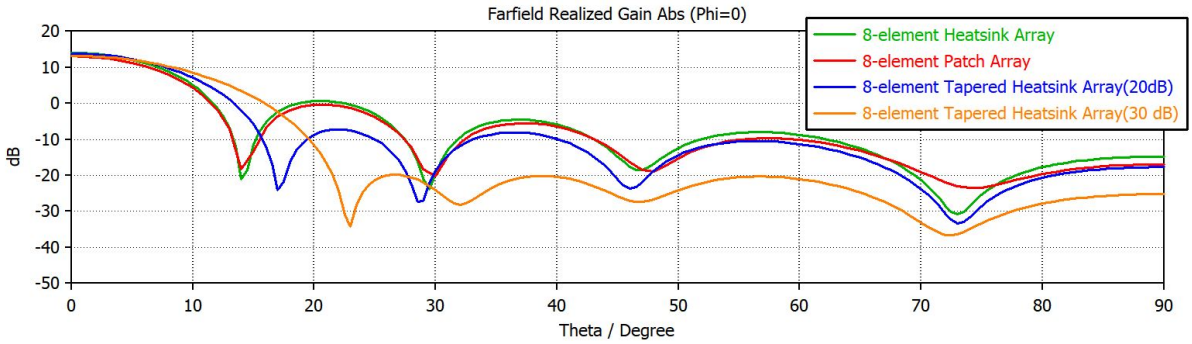

Figure 4.10: Farfield realized gain ($\phi = 0$)

X-oriented antenna array	**Realized Gain (dB)**	**SLL (dB)**	**Junction Temperature** ($^{\circ}C$)
Patch array	13.12	-13.5	124.37
Heatsink array	14.14	-13.4	104.21
Tapered heatsink array (20dB suppression)	13.8	-21.1	104.21
Tapered heatsink array (30dB suppression)	13.2	-33.0	104.21

Table 4.1: Comparison of joint EM-thermal performance

The heatsink array's scanning abilities were investigated by applying appropriate phase shifts between the antenna elements to direct the beam at specified angles. For phase shift calculations, see Appendix **E**. Figure **4.11** shows the realized gain for different scan angles. The x-oriented heatsink array is capable of scanning up to 45 degrees elevation. At 60° elevation angle, the matching is worse and the realized gain goes down to 8.2 dB. The realized gain decreases and the side lobe level increases as the scan angle increases.

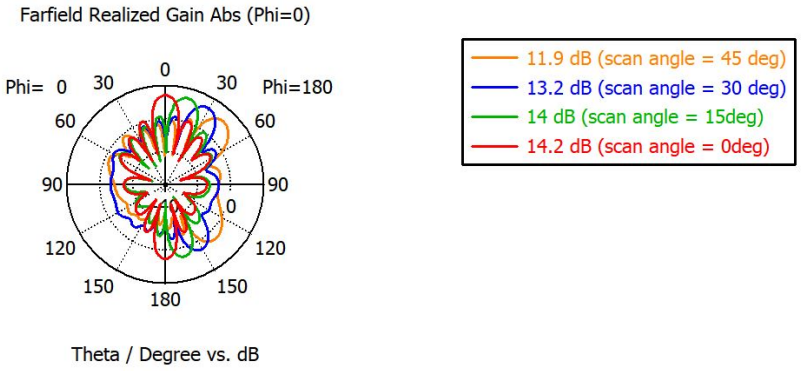

Figure 4.11: Farfield realized gain ($\phi = 0$) for different scan angles

Y-oriented Linear Array

The return loss plots and the realized gain for the y-oriented patch and heatsink array are shown in Figures **4.12** and **4.14**

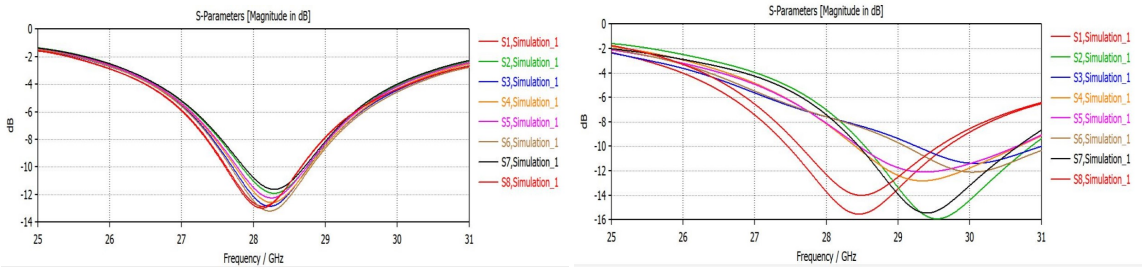

(a) (b)

Figure 4.12: Return loss S11 (dB) of 1 x 8 array,(a)Patch,(b)Heatsink antenna

The middle elements 2-7 resonate at a higher frequency, while 1 and 8 resonate at 28 GHz, as seen in the heatsink array's return loss plot. The patch length for elements 2 to 7 is raised from 2.26 mm to 2.35 mm to shift the resonant frequency, making it a hetreogenous array.

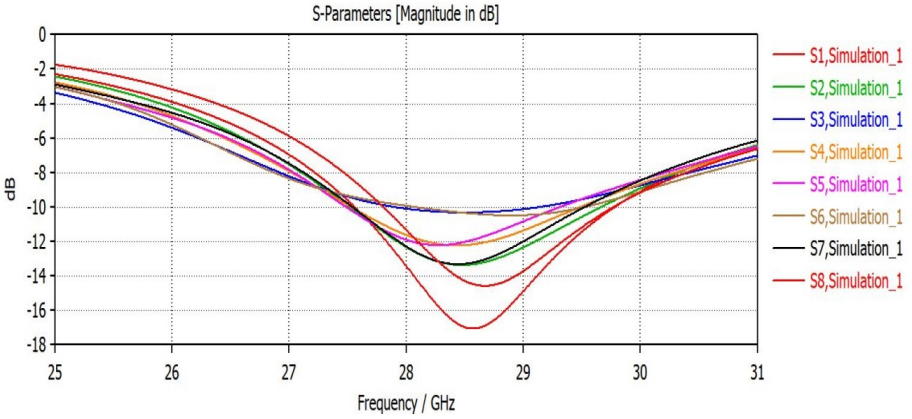

Figure 4.13: Return loss S11 (dB) of 1 x 8 heterogenous heatsink antenna array

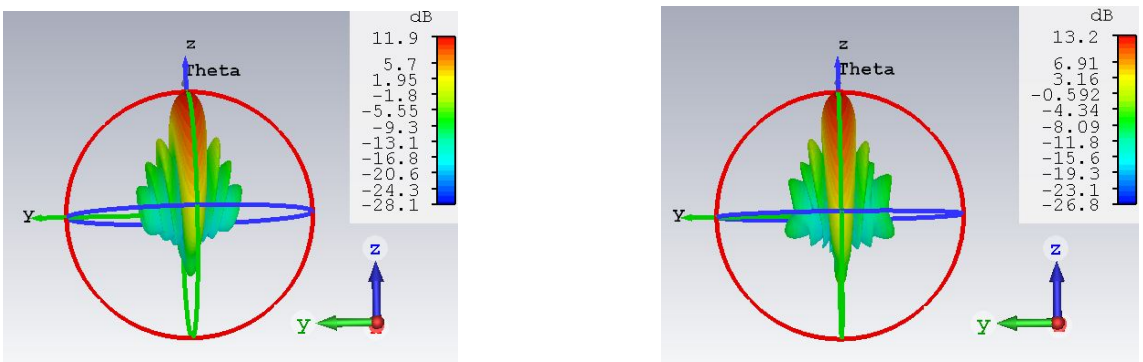

(a) (b)

Figure 4.14: Realized gain (dB), (a) Patch, (b) heatsink antenna

The y-oriented heatsink array achieves a realized gain of 13.2 dB, while the patch array achieves 11.9 dB. The side lobe level for both the arrays are about -13.3dB. Amplitude tapering is applied to reduce this sidelobe further.

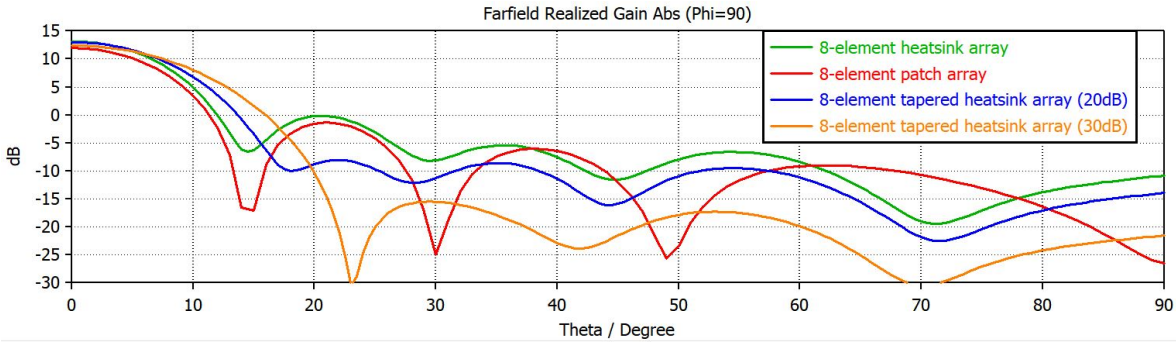

Figure 4.15: Farfield realized gain ($\phi = 90$)

Y-oriented antenna array	**Realized Gain (dB)**	**SLL (dB)**	**Junction Temperature** ($^{\circ}C$)
Patch array	11.9	-13.3	124.37
Heatsink array	13.2	-13.3	104.09
Tapered heatsink array (20dB suppression)	13	-21.0	104.09
Tapered heatsink array (30dB suppression)	12.4	-27.9	104.09

Table 4.2: Comparison of joint EM-Thermal performance

By applying appropriate phase shifts between the antenna elements to direct the beam at specified angles, the scanning abilities of the heatsink array were investigated. The y-oriented heatsink array is capable of scanning up to 30 degrees elevation. At 45° elevation angle, the matching is worse and the realized gain is around 6.5 dB. The realized gain decreases as the scan angle increases.

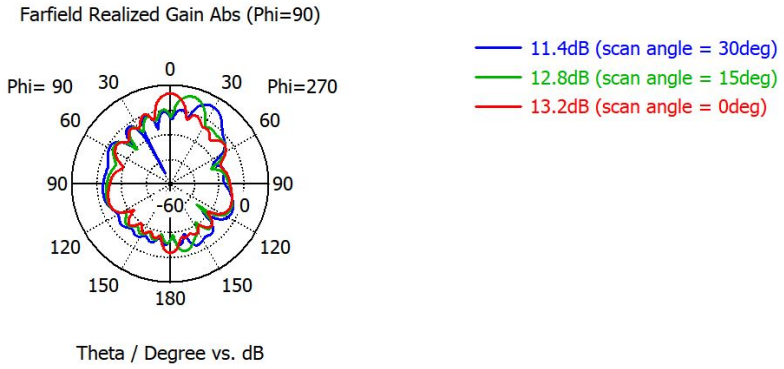

Figure 4.16: Farfield realized gain ($\phi = 90$) for different scan angles

4.2.2. Planar Array Implementation

In this section a 4 x 4, 2D array has been implemented. Figures **4.17**, **4.18**, and **4.19** show the array topology, Return loss and the 3D Realized Gain of the designed patch and heatsink 2D arrays.

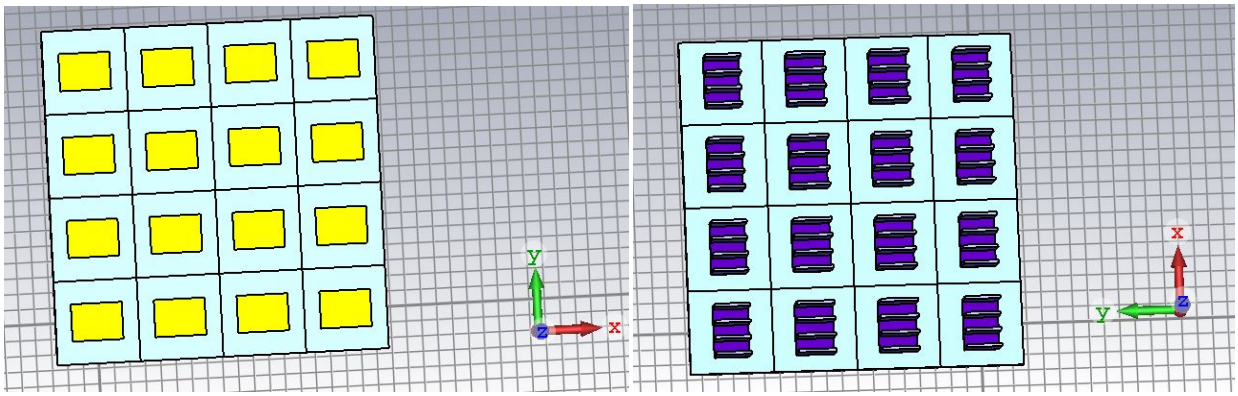

(a) (b)

Figure 4.17: Array topology, (a) 4 x 4 patch, (b) 4 x 4 heatsink

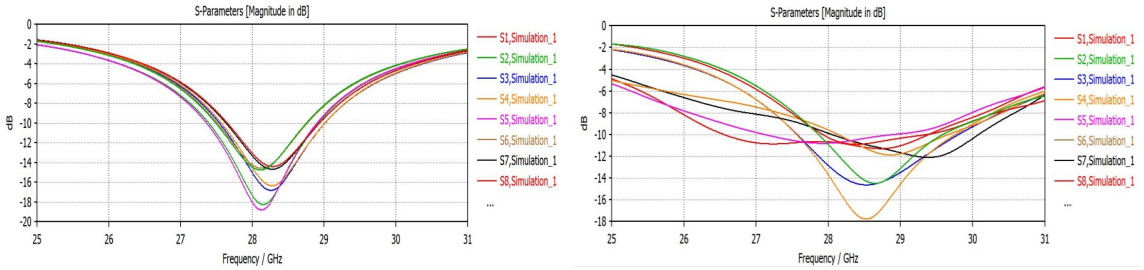

(a) (b)

Figure 4.18: Return loss S11 (dB) of 4 x 4 array,(a)Patch,(b)Heatsink antenna

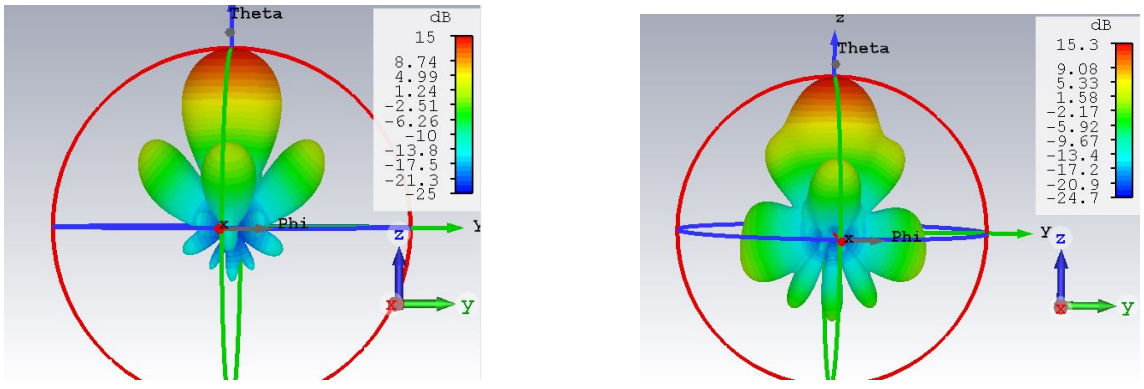

(a) (b)

Figure 4.19: Realized Gain (dB), (a) Patch, (b) heatsink antenna

2D heatsink array designed here is a heterogeneous array with middle elements 5-12 having a patch length of 2.45mm and the other elements with a patch length of 2.26 mm. This is done inorder to shift the resonant frequency near to 28 GHz. The 2D heatsink array provides slighly higher realized gain of 15.3 dB with a comparable side lobe level when compared to the 2D patch array. Amplitude tapering is applied here with 0.5 for the 4 center elements and 1 for the other elements to reduce the side lobe level. The comparison is given in Table **4.3**. The farfield realized gain for both the cut plane $\phi = 0°$ and $\phi = 90°$ are shown in Figures **4.20** and **4.21** and the conduction-based temperature plots for the array are shown in Figure **4.22**. The junction temperature for the tapered heatsink array is the same as that of the non-tapered heatsink antenna array as this is computed under the assumption of no heat power change with modified power amplifier output (which is needed for amplitude tapering).

2D (4 x 4) antenna array	**Realized Gain (dB)**		**SLL (dB)**		**Junction temperature** ($°C$)
	$\phi = 0°$	$\phi = 90°$	$\phi = 0°$	$\phi = 90°$	
Patch array	15	15	-14.2	-13.2	123.2
Heatsink array	15.3	15.3	-13.7	-11.6	108.21
Tapered heatsink array	14.7	14.7	-19.0	-17.2	108.21

Table 4.3: Comparison of joint EM-Thermal performance (4 x 4) array

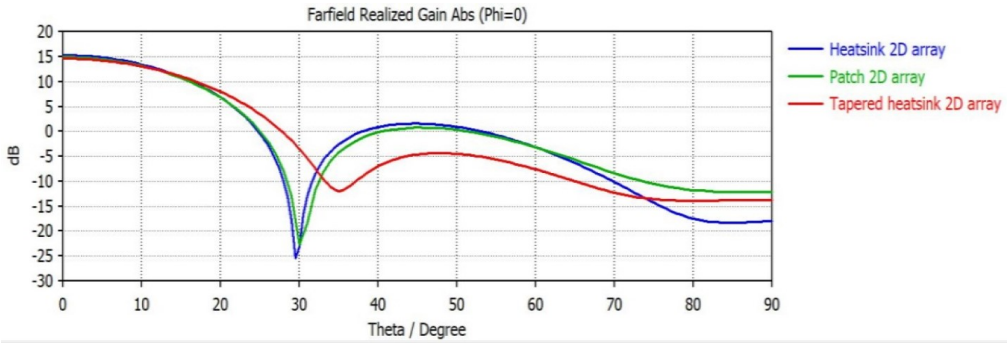

Figure 4.20: Farfield realized gain ($\phi = 0$)

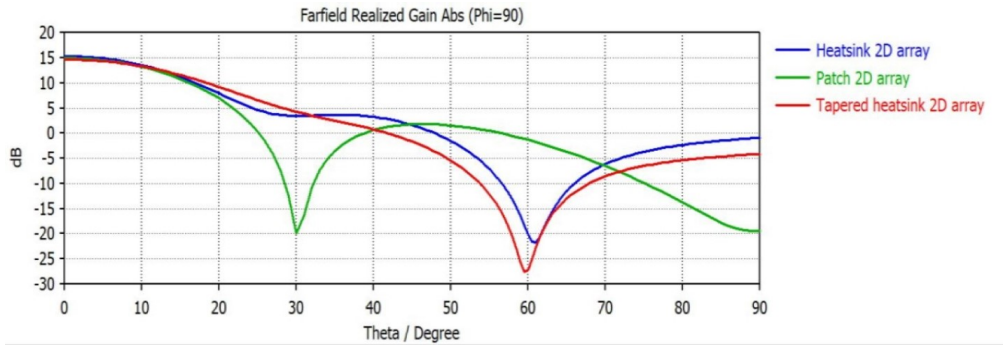

Figure 4.21: Farfield realized gain ($\phi = 90$)

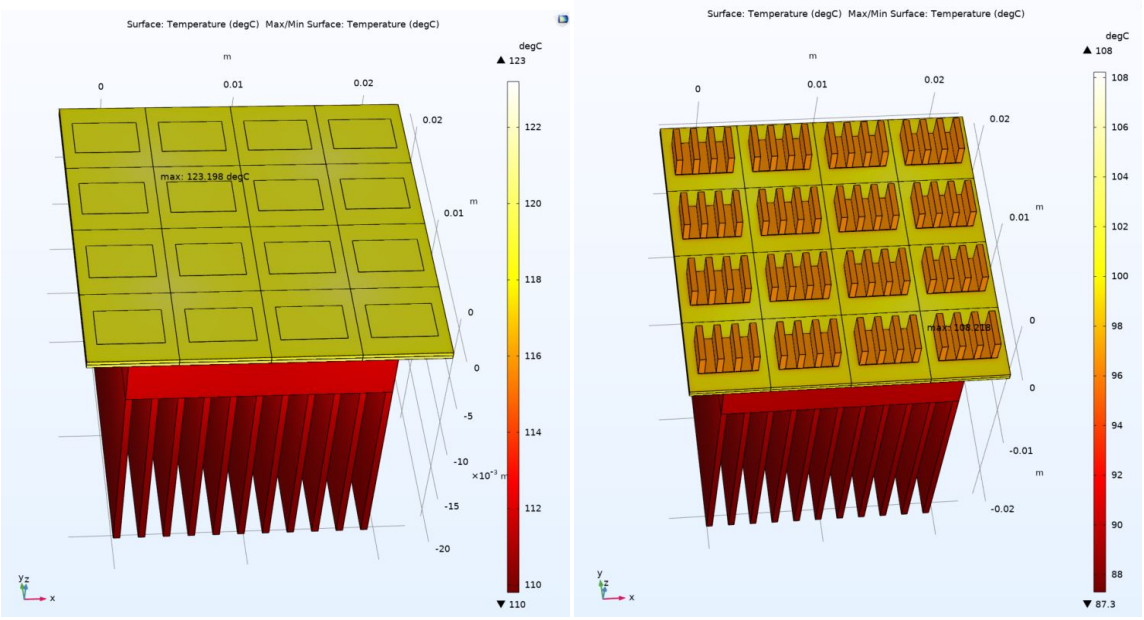

(a) (b)

Figure 4.22: Conduction based model - Temperature plots, 2D array (a)Patch, (b) Heatsink

As a study case, progressive phase shifts are applied for the array to steer the beam at $(\theta_s, \phi_s) = 30°, 45°$. The realized gain for the scanning is shown in Figure **4.23**. The Realized Gain is reduced to 13.9 dB. In case of the array, high cross pol might be amplified by the array gain if the steering angle is in line with the cross pol angle. Otherwise it may be suppressed.

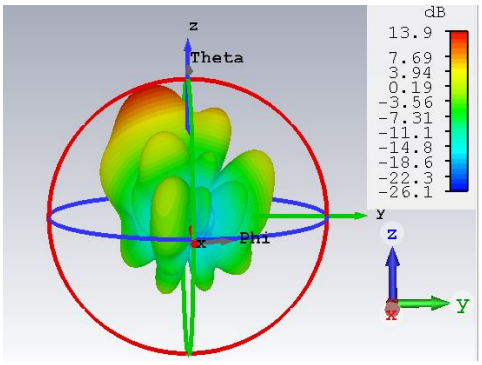

Figure 4.23: 2D Heatsink antenna array with scan angle $(\theta_s, \phi_s) = 30°, 45°$

4.3. Conclusion-Electro-Thermal Aspects

The joint EM and thermal issues are discussed in this chapter. Optimal fin dimensions for array design are chosen based on EM and thermal performance. The results of the conduction-based model show that increasing surface area enhances heat transfer, however in the air flow model, even though the surface area rises, heat transmission does not, and this is due to the fact that the h.t.c also varies in Eq.**3.3**. $N = 4, f_h = 2mm$, and $f_t = 0.2mm$ is chosen as it achieves a good balance between EM and thermal

performance. Both linear (1 x 8) and planar (4 x 4) arrays are implemented. The x-oriented (1 x 8), Y-oriented (1 x 8) and planar(4 x 4) heatsink antenna arrays provided a greater realized gain and heat dissipation with a similar side lobe level when compared with that of the linear patch array. Even for the tapered heatsink antenna case, the realized gain is slightly higher than that of the patch for the linear arrays giving the advantage of low side lobe and low temperature.

5

Conclusions And Future Work

5.1. Conclusion

The goal of this thesis was to design a low-temperature, low-side-lobe mm-Wave heatsink antenna element and its array. The thesis was broken down into four sections. The first section contains a comprehensive literature review of existing antenna thermal management technologies. The heatsink antenna design phase was then completed, with its electromagnetic performance being assessed. The thermal model for the antenna was then included, and the simulated temperature values were compared to those of a standard patch antenna. Finally, suitable heatsink dimensions are chosen for the construction of finite arrays in order to improve their EM and thermal performance.

Thermal management in antennas was divided into three sections: antenna+heatsink, antenna as heatsink, and antenna layout optimization, based on a thorough review of the literature. The majority of antenna thermal management work is done at low frequencies. Due to the growing popularity of mm-Wave design and the importance of heating effects at high frequencies, a few research studies have recently been published. However, with a few exceptions, none of the works provide a proper thermal model that takes into account the relevant chip parameters. Furthermore, the thermal simulations reported in all these research papers are primarily conduction-based or conduction-based with h.t.c assumptions that are typically unknown. **In this thesis, for the first time, a novel mm-Wave heatsink antenna design was developed, complete with thermal modeling and natural convective CFD simulation setup**.

An mm-Wave patch antenna was initially created and a heatsink was placed on top of it to see its effects. Bandwidth, radiation efficiency, and co-pol directivity have all improved. However, in this case, the cross-pol directivity was high. The heatsink base was removed, resulting in a significant increase in co-pol directivity and a modest decrease in cross-pol directivity. Then, different orientations of the rectangular fin and radial pin fin heatsinks was designed and the EM performance was tabulated. The rectangular fins with fins parallel to the patch's non-radiating edges (PNRE) and the Radial pin fins at the patch's center both performed well. As a result, these configurations are

taken into account for additional EM and thermal analysis. Infinite array approximation was used to investigate the impact of these antennas on a very large array. Fins PNRE design was capable of realization in a very large x-oriented linear array with a scan range of ±15°, while the radial fins (center) design was capable of realization in a 2D array with ±60°, according to infinite array approximation employing periodic boundary conditions.

The antenna's thermal model was developed after it was analyzed in terms of EM characteristics. Two-resistor model was investigated, having the necessary beamformer chip features such as heating power, junction-to-board, and junction-to-case resistance values. Because a single beamformer chip can feed four antenna elements, thermal simulations for a four-element (linear or two-dimensional array) were performed. There were two simulation methodologies evaluated. One was a conduction-based model with a convective cooling boundary condition where an h.t.c value is assumed for a natural convective scenario. The other was a natural convective laminar air flow model, in which heat is transferred via gravity. For this simulation, fluid flow and heat transfer physics were coupled, and the h.t.c value was evaluated rather than assumed. Several case studies were conducted using the conduction-based model to examine the effects on junction temperature. The first case study involved increasing h.t.c at the heat source's bottom. The junction temperature was found to be lower when h.t.c was increased. When compared to patch and Radial fins (center) heatsink antennas, the fins PNRE antenna showed greater heat dissipation. The purpose of the second case study was to determine whether the chip's attributes have an impact on thermal performance. The temperature was dropped by $4°C$ when the chip's substrate material was changed from RogersRT5870 to Aluminium Nitride. Heat dissipation was found to be improved by lowering the junction-to-board and junction-to-case resistances. Finally, a case study based on radiative heat transfer was done where the effects of thermal radiation has been observed. In the end, a comparison was made between the two simulation models where it was found that the temperature results were different for the patch antenna. This was due to the difference in heat transfer coefficient values. In the conduction model, the junction temperature of the heatsink antenna array was decreased by $10°C$, while the air flow model revealed a $21.6°C$ degree drop when compared to the patch antenna array.

The major challenge of this thesis was about the trade off between EM and thermal performance of the designed heatsink antenna. As a result, it was critical to choose the right fin dimensions so that the designed antenna has a suitable EM and thermal balance. Parametric study with fin dimensions was made to choose the proper dimensions. The conduction based model results showed decrease in temperature whenever the fin dimension was increased as this increases the surface area. However, the air flow model accounts for the effects on spacing on heat transfer coefficient. Based on the air flow model, the dimensions were chosen for the array design. Both linear and planar arrays were investigated. For the x-oriented (1 x 8), y-oriented (1 x 8) linear arrays, and (4 x 4) planar array the heatsink antenna produced greater realized gain and heat dissipation while maintaining the same side lobe level. This side lobe level was further reduced by amplitude tapering making the heatsink antenna, a low-sidelobe

and low-temperature alternative to the patch antenna.

5.2. Future work

The benefits of designed heatsink antenna in dissipating heat while maintaining good EM characteristics have been emphasized in this thesis. The following are potential future projects that could be pursued as a result of this thesis:

- **Heatsink Antenna Optimization**: Optimum heatsink dimensions are selected only based on the parametric sweep that is done in this thesis. However, this may not be the best as the parametric sweep for one parameter considered here is only a small range while keeping the other parameters constant. Because manual parameter sweeping has limitations, an optimization process must be used to determine near-optimal values for the design parameters. To generate the results, numerous parameters are varied at the same time.

  For the optimization, the critical parameters of the design has to be selected. The values and range of the critical parameters must be given. In our case, the critical parameters would be the fin dimensions and the patch dimensions. Then, geometrical and performance constraints have to be specified. Finally, an optimization goal function has to be selected. The goal function in this situation could be to increase the surface area while keeping the constraints in place. One of the major constraints here would be spacing between the fins as it affects the h.t.c. For this work, we are collaborating with Dr.Bo Liu, Senior Lecturer (Systems Power Energy) at the University of Glasgow, and Dr.Mobayode Akinsolu, Assistant Professor at the Wrexham Glyndwr University who has developed the optimizer. The work has already started where goal function, constraints and critical parameters were selected. We are hoping to finish the optimization to obtain the best parameters for the design that would maximize the surface area and then simulate the design with the conduction and air flow model developed in this thesis to see its thermal performance.

- **Wideband Array**: When a ring is inserted in the air region of the coax, we observed a wide band property for the Y-oriented infinite heatsink array. Impedance matching may be examined further by creating very large finite arrays instead of using Periodic Boundary conditions.

- **Heat Transfer Enhancement**: Due to the antenna substrate's resistance to the majority of heat flow to the antenna side, metallic vias or other thermal enhancement techniques can be used to increase heat flow to the antenna side. For the designed antenna, forced convection with liquid cooling or cooling via external fans can also be tested.

- **Realization Of Aperiodic Heatsink Array**: Aperiodic heatsink arrays can be created at optimized positions instead of amplitude tapering to minimize the side

lobe level. Because the antenna effective aperture is large, this decreases side lobe while maintaining a higher directivity. This larger effective aperture can dissipate more heat than a regular array.

- **Dual-polarized Antenna/Feeding Techniques**: Only single-polarization elements are considered in this thesis, so antenna with dual-polarization can be implemented. Also, different antenna feeding mechanisms can be investigated.
- **Different Heatsink Geometry**: Alternating layout such as the triangular heat sink which can provide better thermal performance can be designed above an antenna and EM performance can be investigated.

A

Extended Heatsink Geometry

Here, the heat fins are extended beyond the patch length (along y) where $L_p = 3mm$ and the fin width (along y) $f_w = 4.5mm$ as shown in Figure **A.1**. The 3D pattern directivity is shown in Figure **A.2**. where several nulls are observed in the distorted pattern with lower directivity compared to when the heatsink geometry is bounded within the patch size.

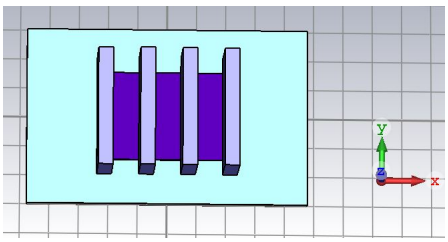

Figure A.1: Extended heatsink geometry (along y)

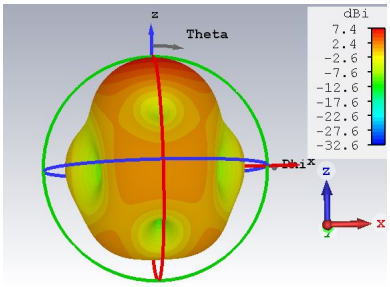

Figure A.2: 3D Pattern Directivity (dBi)

The heatsink geometry extended along x i.e, 5 fins instead of 4 fins exceeding the width of the patch (along x) did not have much impact on the pattern directivity but when the antenna element is reliazed in array the heatfins will be very close to each other causing mutual coupling effects.

B

Calculations For The Thermal Model

The calculations for the assumptions and conditions for the air flow model are provided in this section.

The hydraulic diameter is calculated using Eq.**3.4** for designing the air box and estimating fluid velocity. In contrast to circular pipes, where the hydraulic diameter is simply twice the circle's radius, the hydraulic diameter here is computed using the cross-sectional area and the wetted perimeter. Wetted perimeter is the portion of the perimeter touching the fluid. Figure **B.1** shows the dimensions for the cross-sectional area.

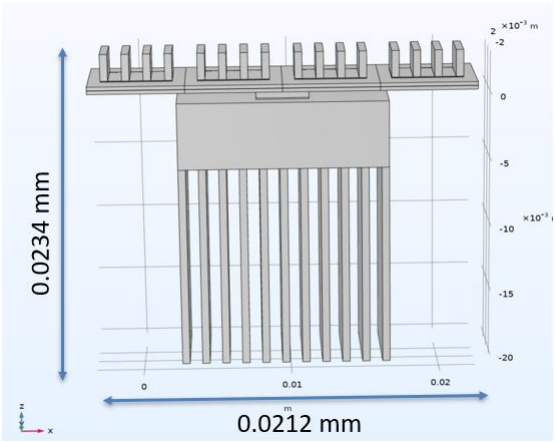

Figure B.1: Cross-section of the heatsink antenna array

Here the cross-section can be taken as a rectangle box and the hydraulic diameter can be calculated as

$$D = \frac{4A}{P} = \frac{4 * lb}{2 * (l + b)} = \frac{4 * 0.0234 * 0.0212}{2 * 0.0446} = 0.0222m \tag{B.1}$$

Based on this, the air box is constructed where the cuboid dimensions are 40 x 114.75 x 40 mm. The fluid velocity and the flow regime is computed. The thermophysical properties of air at 20°C is shown in Table **B.1**

Temp ($^{\circ}C$)	**Density** ρ (kg/m^3)	**Specific heat** $c_\rho(J/Kg.K)$	**Thermal Conductivity** $k(W/m.K)$	**Thermal Diffusivity** $\alpha(m^2/s)$	**Dynamic Viscosity** $\mu(Kg/m.s)$	**Kinematic Viscosity** υ (m^2/s)	**Prandtl Number** Pr
20	1.204	1007	0.02514	2.074 x 10^{-5}	1.825x10^{-5}	1.516x10^{-5}	0.7309

Table B.1: Thermophysical properties of Air

According to [29], typical velocity due to buoyancy force is calculated as

$$U = \sqrt{g\alpha_p \Delta T L} \tag{B.2}$$

where,

g - Acceleration due to gravity = 9.81 $[m.s^{-2}]$
α_p - Coefficient of thermal expansion = 3.43 x 10^{-3} $[K^{-1}]$
L - Hydraulic diameter = 0.0222 $[m]$
ΔT - Typical temperature difference = 343.15 $[K]$

The velocity estimate is found to be $0.5 m/s$ and the simulated velocity slice for the heatsink array shows a closer value of $0.48 m/s$. The velocity slice plot is shown in Figure **B.2**

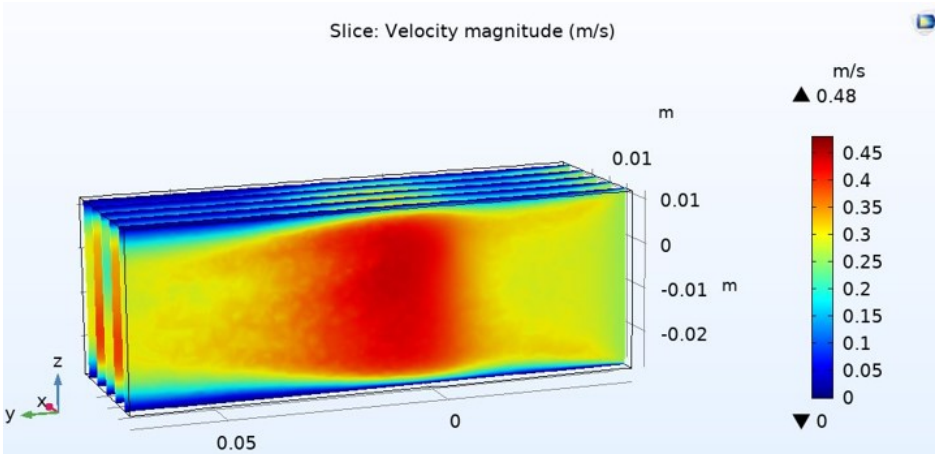

Figure B.2: Velocity slice - heatsink antenna array

The Reynolds number and the Grashof number are used to determine whether the flow is laminar, transitional, or turbulent. The Reynolds number is the ratio of inertial to viscous forces, and it is calculated as follows

$$R = \frac{\rho V D}{\mu} \tag{B.3}$$

where,

R - Reynolds Number
ρ - Fluid density = 1.204 $[Kg/m^3]$
D - Hydraulic diameter or distance = 0.0222 $[m]$
μ - Dynamic Fluid viscosity = 1.825 x 10^{-5} $[Kg/m.s]$

Reynolds number is found to be 697 which means the flow is laminar where the fluid follow smooth path in layers and has a parabolic velocity profile. For R values less than 2000, the flow is laminar and the transition regime is between 2000 and 10^4 [30].

The Grashof number, which is equal to the ratio of buoyant to viscous forces, is given by

$$Gr = \frac{\alpha_p g \Delta T L^3}{\nu^2} \tag{B.4}$$

where,

Gr - Grashof number
α_p - Coefficient of thermal expansion = 3.43 x 10^{-3} $[K^{-1}]$
L - Hydraulic diameter or distance = 0.0222 $[m]$
ΔT - Typical temperature difference = 343.15 $[K]$
ν - Kinematic Viscosity = 1.516 x 10^{-5} m^2/s

For natural convection from vertical flat plates, the transition to turbulent flow occurs in the range $10^8 < Gr < 10^9$. The boundary layer is turbulent at higher Grashof numbers and at lower Grashof numbers, the boundary layer is laminar in the range $10^3 < Gr < 10^6$ [31]. The Grashof number is found to be 5.497 x 10^5 which indicates the flow is laminar.

Having known the flow regime, laminar fluid flow physics is selected in COMSOL and the gravity is activated. To determine the compressibility, Mach number is calculated which is a dimensionless number. It is the ratio of fluid velocity to the velocity of sound.

$$M = \frac{u}{c} \tag{B.5}$$

where,

M - Mach number
u - Fluid velocity = 0.5 $[m/s]$
c - Speed of sound in the medium = 343 $(20^\circ C)$ $[m/s]$

Here, $M < 0.2 - 0.3$ which indicates incompressible fluid flow where material density is constant within the fluid and incompressible Navier-Stokes equation can be used.

C

Extending Ground plane For Heat Transfer

The major part of the heat is transferred through the bottom heatsink attached directly to heat source. Above the chip, the chip substrate and ground plane are highly conductive and then comes the antenna substrate which has lower thermal conductivity of about $0.2 W/m.K$. So, one way to dissipate the heat could be to extend the ground plane and attach heatsink at the bottom of the ground plane as shown in Figure **C.1**

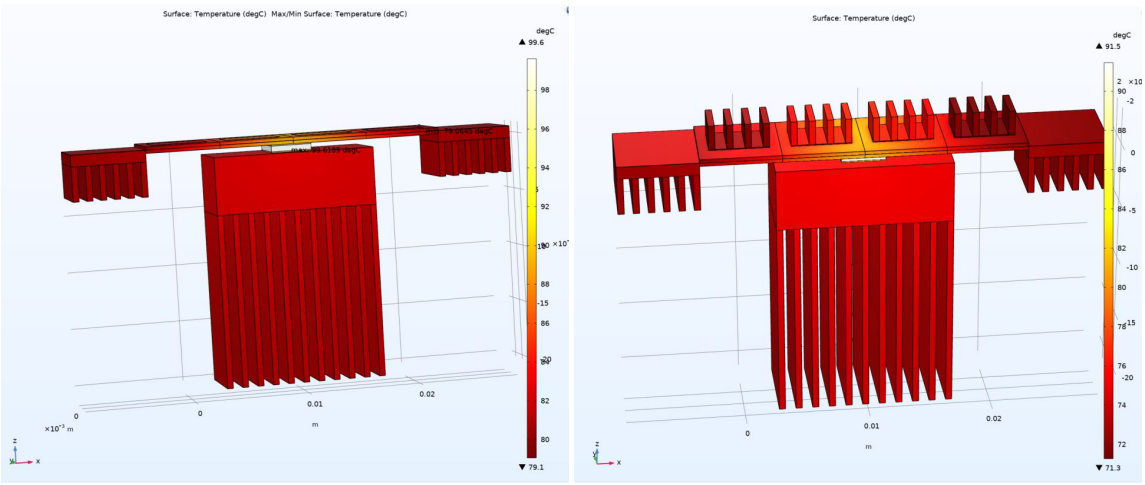

(a) (b)

Figure C.1: Extended groundplane (a) Patch, (b) Heatsink antenna

Extending the ground plane and attaching heatsink at the bottom of the ground plane has reduced the maximum junction temperature from $116°C$ to $99.6°C$ for the patch and from $106°C$ to $91.5°C$ for the heatsink antenna array. The difference in junction temperature between patch and heatsink antenna has been reduced from $10°C$ to $8°C$. This difference will further reduce if you increase the heatsink dimensions at the bottom of the chip or the ground plane as most of the heat flows through it.

D

Additional Parametric Study

Fin thickness (mm)	Number of Fins	Spacing between fins (mm)	Surface area above the patch (mm^2)	Conduction Model (c)	Air flow Model (c)	Co-Pol Dir (dBi)	Cross-Pol Dir (dBi)
0.5	9	0.033	145.98	101.017	107.520	8.873	0.29
0.3	9	0.259	133.09	101.95	107.327	9.025	-0.1916
	10	0.197	147.88	101.33	107.454	8.991	-0.0072
	11	0.147	162.67	100.75	107.393	8.969	0.1116
	12	0.106	177.46	100.18	107.521	9.024	-0.2574
0.1	12	0.325	160.27	101.38	107.217	9.074	-1.636
	16	0.21	213.7	99.51	107.654	8.923	-1.182
	20	0.146	267.12	97.8	107.745	8.944	-0.7938

Table D.1: Parametric study data

E

Amplitude And Phase Shift Calculations

Using Chebwin function in MATLAB, the amplitude values for tapering is obtained. $chebwin(N, SLL)$ is the function where N is the array size and SLL is the suppression factor. The amplitude values are entered in the excitation list in CST. For 20 dB suppression, the amplitude values are $[0.5799, 0.6603, 0.8751, 1.0, 1.0, 0.8751, 0.6603, 0.5799]$ and for 30 dB suppression, the values are $[0.2622, 0.5187, 0.8120, 1.0, 1.0, 0.8120, 0.5187, 0.2622]$.

Progressive phase shifts has to be entered in order to steer the beam to a specific angle. For linear arrays, the progressive phase shift is calculated by Eq.E.1

$$\beta = -kdsin\theta_s \tag{E.1}$$

where,

β - Progressive phase shift between elements
k - Wavenumber = $\frac{2\pi}{\lambda}$ $[m^{-1}]$
d - spacing between elements = 0.5λ $[m]$
θ_s - Scan angle °

β for scan angles $15, 30, 45$, and 60 degrees are calculated as $-46.58, -90, -127.28$ and -155.88 degrees respectively.

Because the steering is in 2D for Planar arrays, the progressive phase shift along x and y is calculated individually using Eq.E.2 and E.3

$$\beta_x = -kd_xsin\theta_scos\phi_s \tag{E.2}$$

$$\beta_y = -kd_ysin\theta_ssin\phi_s \tag{E.3}$$

where,

β_x, β_y - Progressive phase shift between elements along x and y
k - Wavenumber = $\frac{2\pi}{\lambda}$ $[m^{-1}]$
$d_x = d_y$ - spacing between elements along x and y = 0.5λ $[m]$
θ_s, ϕ_s - Scan angle °

For $\theta_s = 30°$ elevation and $\phi_s = 45°$ azimuth, $\beta_x = \beta_y = -63.64°$

Bibliography

[1] 5. Americas, "Understanding mmwave spectrum for 5g networks," *White paper*, 2020.

[2] Y. Aslan, J. Puskely, J. Janssen, M. Geurts, A. Roederer, and A. Yarovoy, "Thermal-aware synthesis of 5g base station antenna arrays: An overview and a sparsity-based approach," *IEEE Access*, vol. 6, pp. 58 868–58 882, 2018.

[3] V. Lakshminarayanan and N. Sriraam, "The effect of temperature on the reliability of electronic components," in *2014 IEEE international conference on electronics, computing and communication technologies (CONECCT)*, IEEE, 2014, pp. 1–6.

[4] B. Döring, "Cooling system for a ka band transmit antenna array," Dec. 2005.

[5] Y. Aslan, C. E. Kiper, A. J. van den Biggelaar, U. Johannsen, and A. Yarovoy, "Passive cooling of mm-wave active integrated 5g base station antennas using cpu heatsinks," in *2019 16th European Radar Conference (EuRAD)*, IEEE, 2019, pp. 121–124.

[6] L. Covert and J. Lin, "Simulation and measurement of a heatsink antenna: A dual-function structure," *IEEE transactions on Antennas and Propagation*, vol. 54, no. 4, pp. 1342–1349, 2006.

[7] L. Covert, J. Lin, D. Janning, and T. Dalrymple, "5.8 ghz orientation-specific extruded-fin heatsink antennas for 3d rf system integration," *Microwave and Optical Technology Letters*, vol. 50, no. 7, pp. 1826–1831, 2008.

[8] ——, "Dual-function 3-d heatsink antenna for high-density 3-d integration," in *2007 IEEE International Workshop on Radio-Frequency Integration Technology*, IEEE, 2007, pp. 26–29.

[9] A. Alnukari, P. Guillemet, Y. Scudeller, and S. Toutain, "Active heatsink antenna for radio-frequency transmitter," *IEEE transactions on advanced packaging*, vol. 33, no. 1, pp. 139–146, 2009.

[10] A. Alnukari, S. Toutain, Y. Scudeller, and P. Guillemet, "Microstrip heatsink antenna for integrated rf transmitters," in *Proceedings of the Fourth European Conference on Antennas and Propagation*, IEEE, 2010, pp. 1–5.

[11] A. Alnukari, Y. Mahe, S. Toutain, and Y. Scudeller, "Microstrip heatsink antenna cooled with sapphire layer for integrated rf transmitters," in *2012 6th European Conference on Antennas and Propagation (EUCAP)*, IEEE, 2012, pp. 1263–1266.

[12] J. J. Casanova, J. A. Taylor, and J. Lin, "Design of a 3-d fractal heatsink antenna," *IEEE Antennas and Wireless Propagation Letters*, vol. 9, pp. 1061–1064, 2010.

[13] M. Rao, N. Oraon, and P. Sravani, "Self assembly based high frequency 3d heatsink antenna," in *2014 IEEE REGION 10 SYMPOSIUM*, IEEE, 2014, pp. 10–14.

[14] S. M. Duffy, G. A. Brigham, K. B. Newman, and J. S. Herd, "Stepped notch antenna array used as a low thermal resistance heat sink," in *2013 IEEE Antennas and Propagation Society International Symposium (APSURSI)*, IEEE, 2013, pp. 622–623.

[15] NEC. (2018). "Antenna heat dissipation technology that enables miniaturization of wireless units for 5g," [Online]. Available: `https://www.nec.com/en/global/rd/technologies/201803/index.html` (visited on 01/22/2021).

[16] Y. Aslan, J. Puskely, A. Roederer, and A. Yarovoy, "Heat transfer enhancement in passively cooled 5g base station antennas using thick ground planes," in *2019 13th European Conference on Antennas and Propagation (EuCAP)*, IEEE, 2019, pp. 1–5.

[17] J. Standard, "Two-resistor compact thermal model guideline," *JESD15-3, JEDEC Solid State Technology Association*, 2008.

[18] J. Park, D. Choi, and W. Hong, "Millimeter-wave phased-array antenna-in-package (aip) using stamped metal process for enhanced heat dissipation," *IEEE Antennas and Wireless Propagation Letters*, vol. 18, no. 11, pp. 2355–2359, 2019.

[19] Y. Aslan, A. Roederer, and A. Yarovoy, "System advantages of using large-scale aperiodic array topologies in future mm-wave 5g/6g base stations: An interdisciplinary look," *IEEE Systems Journal*, 2021.

[20] J. Qian, M. Tang, Y.-P. Zhang, and J. Mao, "Heatsink antenna array for millimeter-wave applications," *IEEE Transactions on Antennas and Propagation*, vol. 68, no. 11, pp. 7664–7669, 2020.

[21] W.-X. Chu, Y.-C. Lin, C.-Y. Chen, and C.-C. Wang, "Experimental and numerical study on the performance of passive heat sink having alternating layout," *International Journal of Heat and Mass Transfer*, vol. 135, pp. 822–836, 2019.

[22] L. Zhou, M. Tang, J. Qian, Y.-P. Zhang, and J. Mao, "Vivaldi antenna array with heat dissipation enhancement for millimeter-wave applications," *IEEE Transactions on Antennas and Propagation*, 2021.

[23] D. Pozar, "Considerations for millimeter wave printed antennas," *IEEE Transactions on antennas and propagation*, vol. 31, no. 5, pp. 740–747, 1983.

[24] S. Shidore, "Compact thermal modeling in electronics design," *Electronics cooling*, vol. 13, no. 2, p. 22, 2007.

[25] Y. Aslan, "Antenna array synthesis and beamforming for 5g applications: An interdisciplinary approach," 2020.

[26] D. Nicholls, *System reliability toolkit*. Riac, 2005.

[27] Gabrian. (2016). "Anodized aluminum heatsinks: What you need to know," [Online]. Available: `https://www.gabrian.com/anodized-aluminum-heatsinks-what-you-need-to-know` (visited on 05/22/2021).

[28] M. Srikanth, "Optimization of vertical heat sink fin spacing for natural convection," in *AIP Conference Proceedings*, AIP Publishing LLC, vol. 2200, 2019, p. 020 054.

[29] C. M. 5.6. (2020). "Buoyancy flow in water," [Online]. Available: https://www.comsol.nl/model/download/819061/models.heat.buoyancy_water.pdf (visited on 06/22/2021).

[30] C. Kothandaraman, *Fundamentals of heat and mass transfer*. New Age International, 2006.

[31] A. Bejan and A. D. Kraus, *Heat transfer handbook*. John Wiley & Sons, 2003, vol. 1.